Effective emergency management prevented larger catastrophe after climate change fueled heavy rains in Central Mississippi river valley

Authors

Ben Clarke, *Centre for Environmental Policy, Imperial College, London, UK*
Friederike Otto, *Centre for Environmental Policy, Imperial College, London, UK*
Izidine Pinto, *Royal Netherlands Meteorological Institute (KNMI), De Bilt, The Netherlands*
Sjoukje Philip, *Royal Netherlands Meteorological Institute (KNMI), De Bilt, The Netherlands*
Joseph Giguere, *Climate Central, Princeton, NJ 08542, USA*
Shel Winkley, *Climate Central, Princeton, NJ 08542, USA*
Bernadette Woods-Placky, *Climate Central, NJ 08542, USA*
Wenchang Yang, *Department of Geosciences, Princeton University, Princeton, NJ 08544, USA*
Robert Vautard, *Institut Pierre-Simon Laplace, Paris, France*
Nick Baumgart, *Copenhagen Centre for Disaster Research, Global Health Section, Department of Public Health, University of Copenhagen, Copenhagen, Denmark*
Emmanuel Raju, *Copenhagen Centre for Disaster Research, Global Health Section, Department of Public Health, University of Copenhagen, Copenhagen, Denmark; African Centre for Disaster Studies, North-West University, South Africa*

Review authors

Clair Barnes, *Centre for Environmental Policy, Imperial College, London, UK*
Joyce Kimutai, *Centre for Environmental Policy, Imperial College, London, UK*
Sjoukje Philip, *Royal Netherlands Meteorological Institute (KNMI), De Bilt, The Netherlands*
Geert Lenderink, *Royal Netherlands Meteorological Institute (KNMI), De Bilt, The Netherlands*

Main findings

- The floods inundated large rural areas including agricultural fields, especially in Arkansas which has resulted in an estimated 78 Million USD of damage due to losses in fields that were already planted. Larger losses were avoided due to the timing of the floods before other crops like peanuts and cotton were planted, and since there is still a window to replant crops like corn and soybeans.
- Based on gridded data products, we find that the extreme rainfall event over the study region is relatively rare, expected to occur in today's climate only once every 90-240 years across different observational and reanalysis datasets. However, in a 1.3°C cooler climate, extreme rainfall such as observed would be even rarer. The best estimates for the increase in likelihood for the 2025 event associated with this warming is between a factor 2 to 5, and the increase in intensity for an event of equivalent rarity as observed is 13-26%.
- To quantify the role of human-induced climate change in this increased likelihood and intensity we also analyse climate model data over the study region for the historical period. The best estimate of the synthesised result, combining observations with climate models, is about a 40% increase in likelihood and about a 9% increase in intensity. These estimates are smaller than the observed trends due to large discrepancies between the climate model results. While some models show increases similar to or larger than the observed trends, others show weaker or even decreasing trends.
- In contrast, climate models consistently project that extreme precipitation events such as the one observed in April 2025 will become more frequent and intense in the future as global temperatures rise. Under current climate policies - which will lead to warming of approximately 2.6°C by 2100 - such extremes are expected to approximately double in likelihood again, and increase in intensity by about a further 7%.
- As the moisture that fuelled the rainfall event was partly coming from the Gulf of Mexico we also assessed the role of climate change in the sea surface temperatures. We found that these waters were heated by approximately 1.2 °C (2.2 °F) due to human-caused climate change, and such ocean conditions are now about 14 times more likely than in a cooler pre-industrial world. This contributed to higher evaporation rates, increasing the availability of moisture in the rainfall event.
- The strong observed trends in precipitation extremes in this region are also found in other studies using different methods, across different regions, including the Central Mississippi river valley and are assessed as being attributable to climate change by the IPCC AR6 report.
- In conclusion, due to (1) the observed trends that are (2) in line with IPCC assessments and other literature in the region, and (3) the clear emergence of a climate change signal with further warming in all climate models as well as (4) the availability of more moisture due to higher SSTs, we state that climate change amplified the heavy rainfall leading to the floods and that the estimate from observations and models combined of a 9% increase in intensity and 40% increase in likelihood is conservative and the role of climate change could be as large as the observations alone suggest.
- Despite being an extremely complex event, with tornadoes, flash floods, riverine floods and landslides overlapping, the US National Weather Service (NWS) made a tremendous effort to provide early warnings for the floods, in some cases up to a week in advance of river crests. These early warnings allowed state and local emergency departments to prepare, inform the public, and evacuate those at highest risk. While any loss of life is devastating, the outcomes

of this event point to the effectiveness of decades-long investments made in forecasting, early warning systems, and forecast-based action.

- Nearly half of NWS field offices are facing vacancy rates of 20% or more, double the short-staffing levels of a decade ago. Former NWS leaders have recently warned that layoffs could impact the ability of NWS offices to respond to extreme weather events and keep people safe.

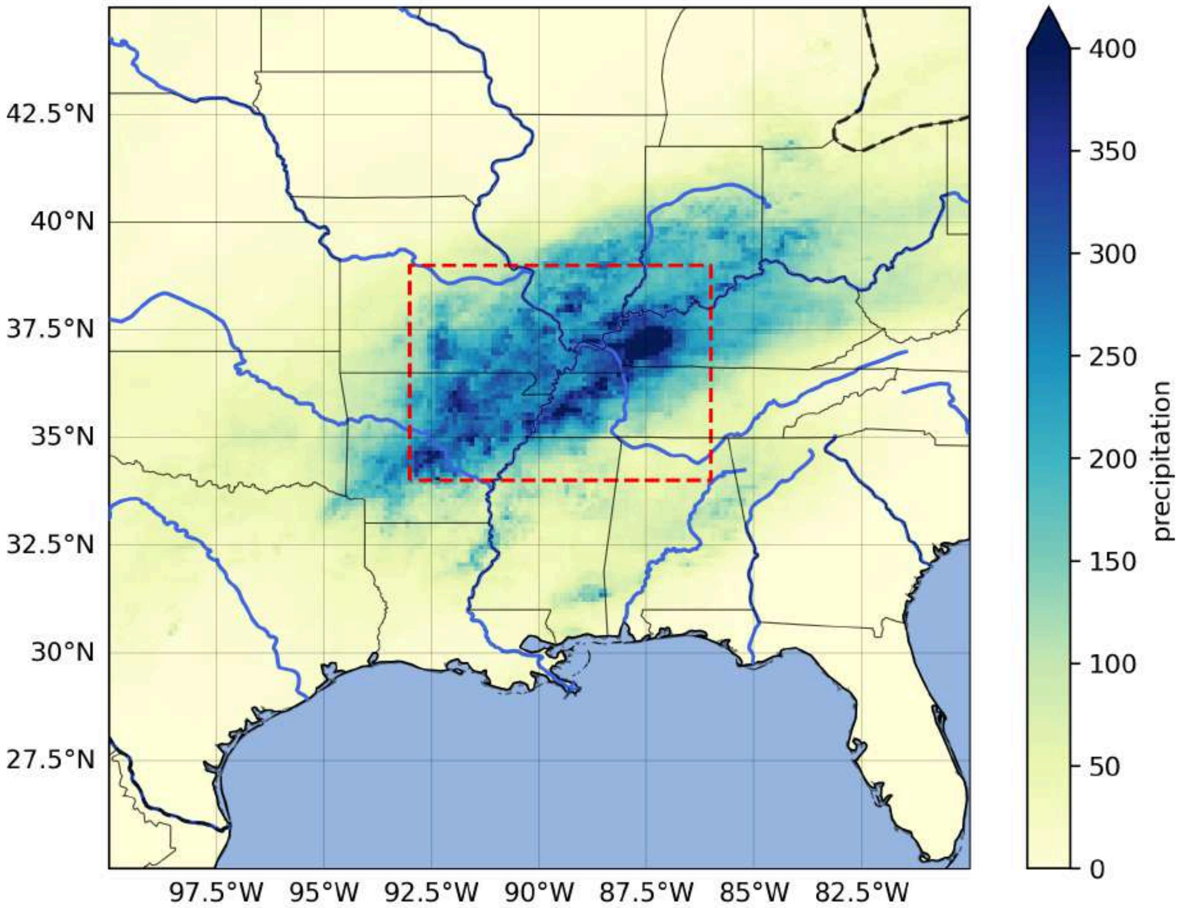

Figure 1.1: *4-day accumulated precipitation over the eastern central US from 03/04/2025-06/04/2025. Major rivers are marked in blue and the study region for rainfall is highlighted with the red dashed line. Data from MSWEP.*

1 Introduction

At the beginning of April 2025, large parts of the southern Midwest and Southeastern parts of the US experienced extremely heavy rainfall between the 3rd and 6th of April, as well as a record number of tornado warnings on the 2nd of April leading to widespread flooding in parts of Mississippi, Arkansas, Missouri, Illinois, Indiana, Kentucky, Tennessee and Alabama, that have been called "historic" or "generational" (Holthaus, 2025). Over the four days, more than 400 mm (16 inches) of rain fell in some areas (Fig. 1.1), with devastating consequences.

24 fatalities have been reported, approximately 9 of which were directly due to tornados (Storm Prediction Centre, 2025), with a significant portion of the casualties occurring in Tennessee, where at least 10 lives were lost. Missouri accounted for 3 deaths, while Kentucky saw 2 fatalities (ABC News, 2025). Tennessee, Kentucky and Arkansas declared a state of emergency (FEMA, 2025). Additionally, one person died each in Indiana, Arkansas, and Mississippi. Early estimates of total economic damages from the event are between \$80 - \$90 billion (AccuWeather, 2025). Power lines were also brought down, leaving over 100,000 customers without electricity in Arkansas and "thousands" in Tennessee (NYT, 2025).

Meteorologically, the heavy rainfall was caused by a strong pressure gradient between a high-pressure system positioned over the East Coast and Southeastern United States and a low-pressure system to the west. The boundary between these contrasting air masses remained nearly stationary, leading to a so-called stalled front, which helped organize training thunderstorms and heavy rainfall. While this front contributed to a favorable, unstable environment for severe weather, a series of atmospheric disturbances triggered the development of a mesoscale convective system (MCS) responsible for the severe thunderstorms and tornadoes. An influx of upper-level moisture from the eastern Pacific, carried by the southwest jet stream, combined with surface moisture from the Gulf of Mexico, where sea surface temperatures (SSTs) were exceptionally high, enhanced convective available potential energy (CAPE), providing additional fuel for storm development. Prior to the event, the National Weather Service reported above-normal soil moisture across much of the region due to late winter precipitation, which likely exacerbated the flooding impacts (National Weather Service, 2025). The combination of elevated moisture at both upper and lower levels of the atmosphere created favorable conditions for the intensification of severe weather, including repeated supercell thunderstorms in the mid-Mississippi valley, the main cause for both the tornado outbreaks and the extreme rainfall.

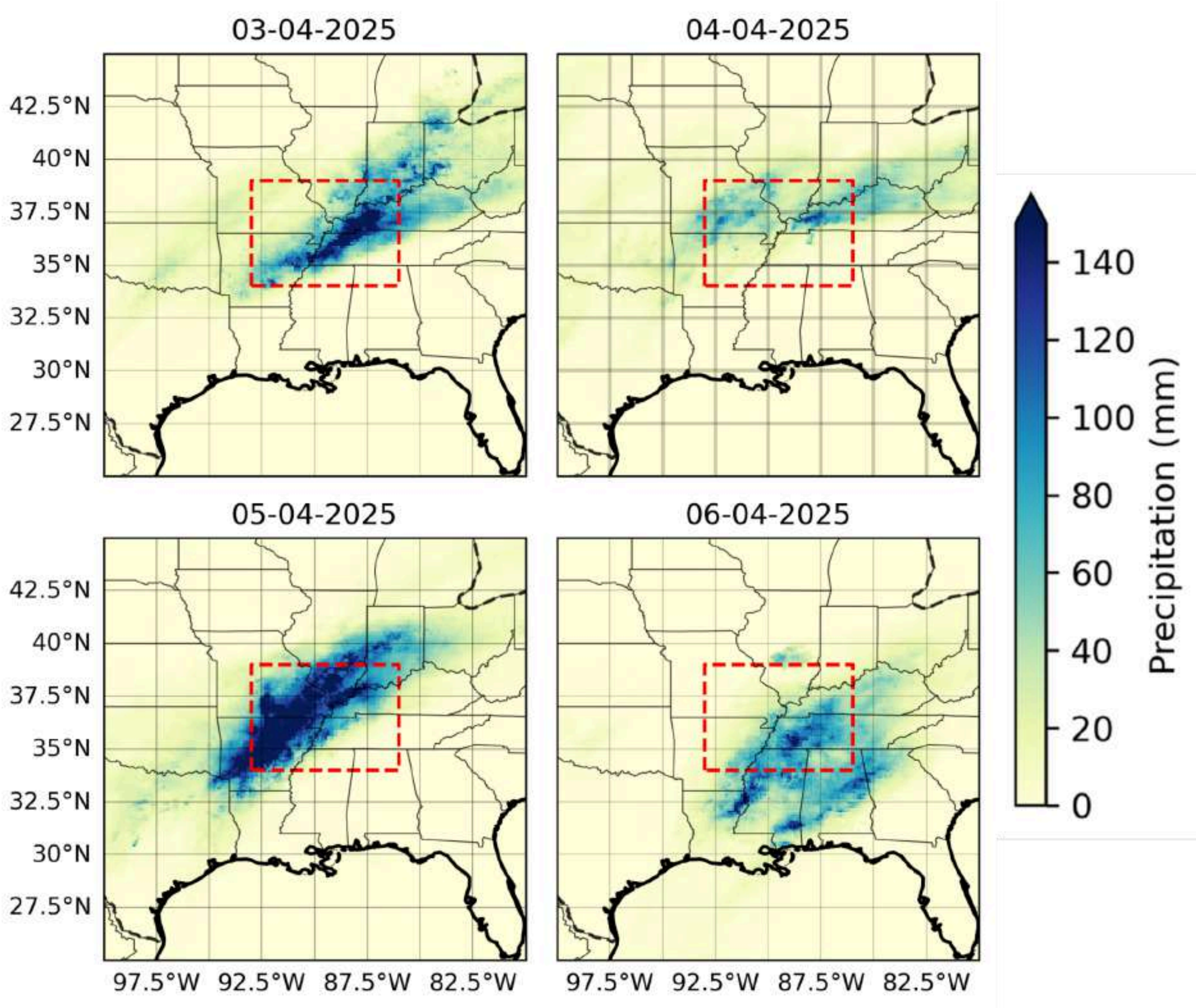

Figure 1.2: *Daily precipitation over the Midwest, central and southern US from 3rd-6th April 2025. Data: MSWEP.*

1.1 Rainfall extremes in the central US

The IPCC's AR6 report assesses an increasing trend in precipitation extremes across both regions that encapsulate the study region. In Eastern North America (ENA), the trend is categorized as *low confidence,* in Central North America (CNA) the trend is assessed to have *medium confidence* on its attribution to human influence. It is important to highlight that the difference in confidence is not related to a difference in the strength of the trends, but to the difference in availability of evidence - and in particular attribution studies - at the time of writing of the 6th assessment report. This gives important context for this study, both the existing evidence of increasing trends and the need for further study. However, since then more literature has also been published. Wallace et al., (2025) find a robust intensification of mesoscale convective systems (MCSs) in spring over most of the eastern US, due to changes in the large-scale circulation that facilitate transport of warmer moister air. Additionally, Ramseyer et al (2022) found an increasing trend in both the size and intensity of atmospheric rivers originating in the Gulf of Mexico.

In a review paper on MCSs, Schumacher and Rasmussen (2020) find that rainfall associated with MCSs is increasing with high confidence, accompanied by changes in several other factors. The speed of motion is expected to rise, but with low confidence, while the size of storms was found to increase with medium confidence, and the frequency of environmental conditions conducive to the formation of MCSs was found to grow, albeit with low confidence. They did not identify changes in wind speeds and storm organization. These changes are assessed to be primarily driven by increases in atmospheric moisture and instability, both of which are projected with high confidence. Additionally, convective inhibition was assessed to rise with medium confidence, which could affect storm development. There is low confidence in the increasing frequency of environmental conditions that support MCSs, while changes to vertical wind shear remain uncertain. These mechanisms, the strengthening of the low level jet and intensified moisture transport are analysed in detail in Prein et al., (2017) and Feng et al., (2016).

Looking at various extreme precipitation indices globally, Dong et al., (2021) find an attributable increase in extreme rainfall in the Eastern and Central parts of North America, corroborating that observed trends (Chinita et al., 2021) are indeed due to human-induced climate change. While there are no attribution studies focussing on extreme rainfall specifically caused by MCSs, many studies have attributed the rainfall associated with tropical cyclones in the Southeastern region of the US, all finding independent of the methods used or events studied a strong increase in heavy precipitation, often beyond what is expected from the Clausius-Clapeyron (CC) relationship alone (Wehner et al., 2021; Reed et al., 2022; Reed et al., 2023; van Oldenborgh et al., 2017; Risser and Wehner, 2017). One possible mechanism behind this 'super-CC scaling', even at synoptic scales, is dynamical amplification. As the thermodynamic component of global warming results in higher moisture totals and precipitation rates, this in turn may cause a greater release of latent heat, further amplifying vertical ascent and thus amplifying precipitation further (Nie et al., 2018; Lenderink et al., 2017).

1.2 Event Definitions

1.2.1 Extreme rainfall in Central Mississippi Valley

From December 2024-February 2025, the central Mississippi Valley region experienced above average precipitation, leading to high soil moisture into spring (National Weather Service, 2025). From 3rd-6th April, 2025, the central Mississippi Valley region experienced sustained and widespread rainfall, which was the wettest 4-day period ever recorded in the region and led to extensive flooding across the region (Fig. 1.3). This rainfall occurred along an extended stalled front between high pressure in the east and low pressure to the west. Along this front, conditions were highly conducive to supercell thunderstorms due to the abundant warmth and moisture, and high atmospheric instability. This resulted in a major tornado outbreak, and may have driven extreme localized rainfall. It remains unclear exactly which elements of the flooding-related impacts were driven by intense short-duration (sub-daily) rainfall from localised convective systems, compared to the widespread extended (multi-day) precipitation accumulations due to the large-scale movement of air masses. Nonetheless, the following factors are clear. Moderate to major flooding occurred on most rivers in the affected region. The rainfall totals over the wider region were exceptional. It is also evident that the atmospheric configuration favoured the convergence of surface moisture from an unusually warm Gulf of Mexico (Figs. 1.4 & 1.5), and upper level moisture from the eastern Pacific along the southwest jet (Figs. 1.4 & 1.6).

We therefore analyse the 4-day rainfall totals over the central Mississippi Valley, acknowledging that this event definition does not capture extreme local rainfall rates or tornado-related impacts, but does capture the scale of the flooding and the effects of this 'perfect storm' atmospheric configuration. Further, we limit the study to March-May extremes due to the strong evidence for the intensification of precipitation extremes during this season, described above (Wallace et al., 2025), and the seasonality of such extremes evident in the seasonal cycles of precipitation (Fig. 1.3). Finally, we separately assess the role of climate change in the warm SSTs in the Gulf of Mexico, which was the source of much of the precipitated moisture.

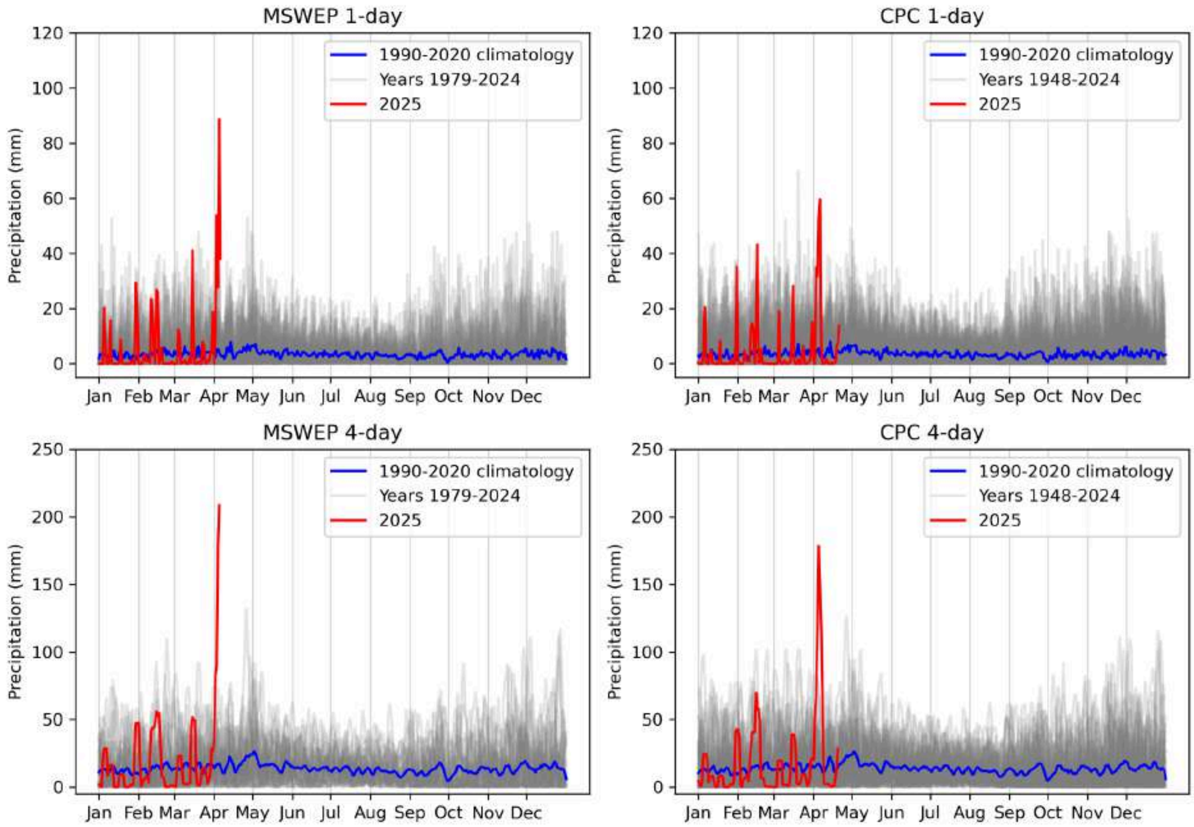

Figure 1.3: *Seasonal cycles of precipitation over the study region in two observational/reanalysis datasets, MSWEP and CPC, for 1- (top) and 4-day (bottom) accumulations. Each year in the record is shown in grey, the 1990-2020 climatology in blue, and 2025 daily data in red.*

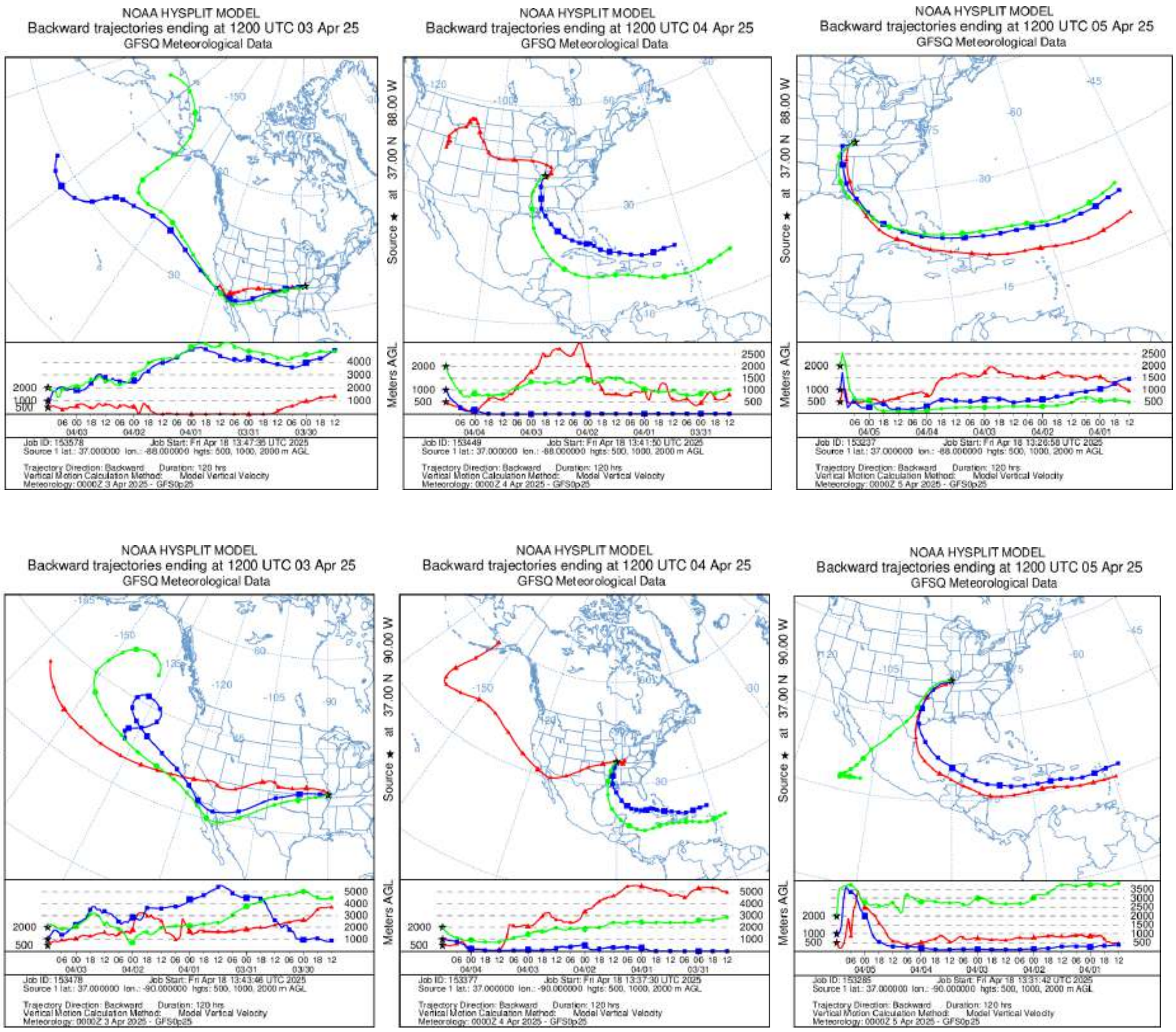

Figure 1.4: *Back-trajectories for air masses at two points within the study region, 88 W - 37 N (top) and 90 W - 37 N (bottom), ending on 03-05/04 at 12:00 UTC each day, from the NOAA HYSPLIT model. Red, blue and green lines show the back trajectories for 500, 1000 and 2000 m above ground level, respectively. Each marker represents a step of 6h back in time.*

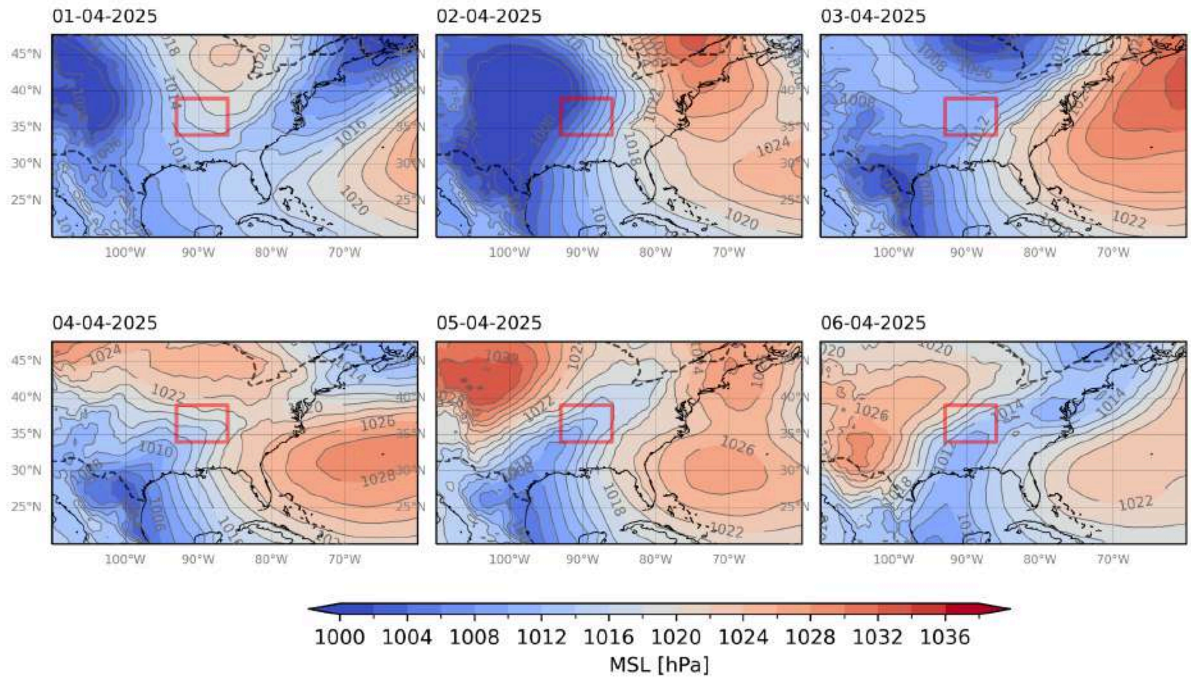

Figure 1.5: *Mean sea level pressure from 1st-6th April 2025 over the eastern US. The study region is highlighted in red. Data: ERA5.*

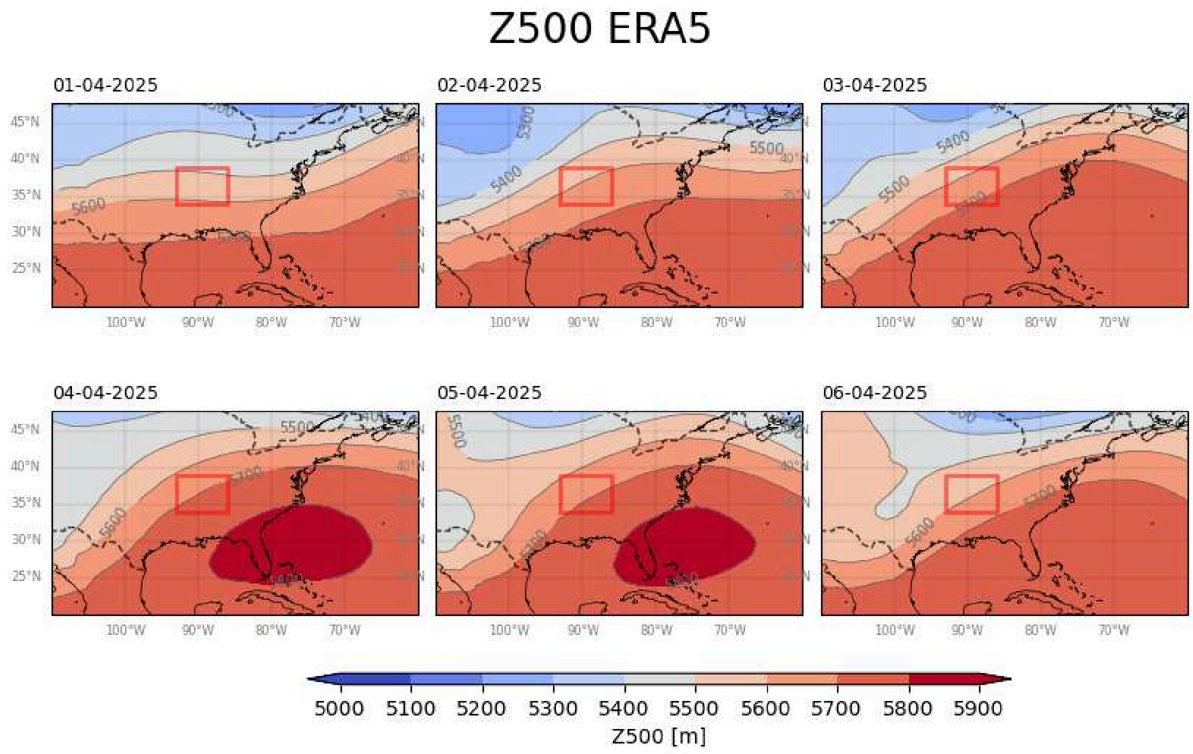

Figure 1.6: *500 hPa geopotential height from 1st-6th April 2025 over the eastern US. Data: ERA5.*

1.2.2 Summary of event definitions

In this study, we aim to analyse changes in the conditions that resulted in the widespread flooding-related impacts from this event. That includes the extreme precipitation that drove the impacts, and also the high sea surface temperatures (SSTs) in the Gulf of Mexico with a high pressure at upper levels (Fig. 1.6) and low surface pressure over the study region (Fig. 1.5) that resulted in a significant influx of moisture into the region via an enhanced atmospheric river. To do so, we use two event definitions:

- **Extreme rainfall, rx4day** - the March-May maximum of 4 day accumulated rainfall, averaged over the central Mississippi valley, bounded by 86-93°W, 34-39°N (Fig. 1.1)
- **Gulf of Mexico SSTs** - the Ocean Climate Shift Index, aggregated over two days across the Gulf of Mexico (bounded by 81°W to the east, 18°N to the south) (Fig. 3.1)

Using these two event definitions, we assess the influence of anthropogenic climate change on the events of April 2025 by comparing the likelihood and intensity of similar extremes at present with those in a 1.3°C cooler climate. For the extreme precipitation index, rx4day, we also extend this analysis into the future by assessing the influence of a further 1.3°C of global warming from the present climate. This is in line with the latest Emissions Gap Report from the United Nations Environment Programme, which shows that the world is on track for at least 2.6°C temperature rise given currently committed policies (UNEP, 2024).

2 Extreme rainfall attribution using WWA protocol

2.1 Data and methods

2.1.1 Observational data

We first use observational and reanalysis data to estimate the return period of a similar event in the present day and to assess the historical trends with increasing GMST. The datasets used are as follows:

1. **ERA5** - The European Centre for Medium-Range Weather Forecasts's 5th generation reanalysis product, ERA5, is a gridded dataset that combines historical observations into global estimates using advanced modelling and data assimilation systems (Hersbach et al., 2020). We use daily precipitation data from this product at a resolution of 0.25°×0.25°, from the years 1950 to present. The re-analysis is available until the end of the preceding month (March 2025). We extend the re-analysis data with the ECMWF analysis (up to 6th April 2025).
2. **CPC** - We use CPC daily precipitation. This is the gridded product from NOAA PSL, Boulder, Colorado, USA known as the CPC Global Unified Daily Gridded data, available at 0.5° x 0.5° resolution, for the period 1979-present. Data are available from NOAA.

3. **MSWEP** - The Multi-Source Weighted-Ensemble Precipitation (MSWEP) v2.8 dataset (updated from Beck et al., 2019) is fully global, available at 3-hourly intervals and at 0.1° spatial resolution, available from 1979 to ~3 hours from real-time. This product combines gauge-, satellite-, and reanalysis-based data, including ERA5.
4. **nClimGrid-Daily** - We use the NCEI's nClimGrid-Daily product, version v1.0.0, which contains gridded fields and area averages of daily maximum, minimum, and average temperatures (Tmax, Tmin, and Tavg) and daily precipitation amount (Prcp) for the Contiguous United States (CONUS) from January 1, 1951–present. Data are derived from morning and midnight observations from the Global Historical Climatology Network-daily (GHCNd) dataset, and are available from NOAA.
5. **GHCN-D -** We use local stations from the Global Historical Climatology Network daily (GHCNd), an integrated database of daily climate summaries from land surface stations across the globe. We use time series of daily precipitation from stations at locations (IDs): Benton (USC00030582), Eldon (USC00232503), Oolitic Purdue (USC00126580), Guntersville (USC00013573), and Union City (USC00409219), where there are at least 70 years of data with no gaps of more than one year in the rx4day time series, and with values in at least 90% of years. Single missing values in the rx4day time series are linearly interpolated. Data are available from NOAA.

Finally, as a measure of anthropogenic climate change we use the (low-pass filtered) global mean surface temperature (GMST), where GMST is taken from the National Aeronautics and Space Administration (NASA) Goddard Institute for Space Science (GISS) surface temperature analysis (GISTEMP, Hansen et al., 2010 and Lenssen et al. 2019).

2.1.2 Model and experiment descriptions

We use 3 multi-model ensembles from climate modelling experiments using very different framings (Philip et al., 2020): Sea Surface temperature (SST) driven global circulation high resolution models, coupled global circulation models and regional climate models.

1. Coordinated Regional Climate Downscaling Experiment (CORDEX) - North America (CORDEX-NAM) data archive contains output from regional climate models (RCMs) run over a domain covering most of North America using boundary conditions from global climate model (GCM) simulations in the CMIP5 archive. These simulations run from 1950–2100 with a spatial resolution of 0.22°/25km or 0.44°/50km (Mearns et al., 2017), composed of historical simulations up to 2005, and extended to the year 2100 using the RCP8.5 scenario.

2. HighResMIP SST-forced model ensemble (Haarsma et al. 2016), the simulations for which span from 1950 to 2050. The SST and sea ice forcings for the period 1950-2014 are obtained from the 0.25° x 0.25° Hadley Centre Global Sea Ice and Sea Surface Temperature dataset that have undergone area-weighted regridding to match the climate model resolution. For the 'future' time period (2015-2050), SST/sea-ice data are derived from RCP8.5 (CMIP5) data, and combined with greenhouse gas forcings from SSP5-8.5 (CMIP6) simulations (see Section 3.3 of Haarsma et al. 2016 for further details).

3. The FLOR (Vecchi et al., 2014), AM2.5C360 (Yang et al., 2021, Chan et al., 2021) and AM2.5 (Yang et al., 2021) climate models are developed at Geophysical Fluid Dynamics Laboratory (GFDL). The FLOR model is an atmosphere-ocean coupled GCM with a resolution of 50 km for land and atmosphere and 1 degree for ocean and ice. Ten ensemble simulations from FLOR are analysed, which cover the period from 1860 to 2100 and include both the historical and RCP4.5 experiments driven by transient radiative forcings from CMIP5 (Taylor et al., 2012). Both AM2.5C360 and AM2.5 are atmospheric GCMs based on that in the FLOR model (Delworth et al., 2012, Vecchi et al., 2014) with a horizontal resolution of 25 and 50 km, respectively. Three ensemble simulations of the Atmospheric Model Intercomparison Project (AMIP) experiment (1871-2100) from each of the two models are analysed. Radiative forcings are using historical values over 1871-2014 and RCP4.5 values after that. For each model, simulations are initialised from three different pre-industrial conditions but forced by the same SSTs from HadISST1 (Rayner et al., 2003) after groupwise adjustments (Chan et al., 2021) over 1871-2020. AM2.5C360 SSTs between 2021 and 2100 are using the FLOR RCP4.5 experiment 10-ensemble mean values after bias correction, while AM2.5 SSTs are using the first ensemble member values after bias correction.

2.1.2.1 Performance of Global and Regional Climate Models

In this event the rainfall was driven by both the synoptic-scale stalled front, with moisture moving in from the Gulf of Mexico, and several embedded tornado-generating supercells. The rainfall fell over 4 days and hundreds of kilometres along the front. The climate models used here clearly cannot simulate the individual storms, but we are running this analysis on the basis that most of the rainfall was driven by the synoptic interactions and, for the convective element(s) of the event, that the parametrisations perform reasonably well at this scale.

We are primarily using CORDEX NAM-22 models (~25 km resolution), described above, which have been assessed by a few papers in their representation of MCSs. In general, they have enhanced mesoscale process with respect to the 0.44° ensemble (Meyer et al., 2021), though they are known to underestimate the occurrence of high intensity precipitation events in summer due to the convective parametrisation (Diaconescu et al., 2017). The largest biases in precipitation with respect to observed reference datasets are now over the Pacific North West (PNW) and Midwest, and are related to orographic effects (Souleymane et al., 2022). It is clear that these RCMs still do not adequately capture local extreme rainfall driven by small-scale convective processes (Nazarian et al., 2022; Prein et al., 2020), but are acceptable for extremes driven by large-scale circulation modes, more common in winter and spring in the region (Picard et al., 2023, Prein et al., 2019).

Similarly, HighResMIP models (~25-50 km resolution) present an improvement over coarser CMIP6 GCMs in many key precipitation-generating phenomena, such as atmospheric rivers, extratropical cyclones and mesoscale convective systems (Priestly & Catto, 2022; Michalek et al., 2023), though major challenges remain for sub-grid-scale phenomena (<25 km) (Michalek et al., 2023).

Lenderink et al., 2025 show for hourly precipitation that, compared to RCMs, Convection Permitting Models (CPMs) produce better overall rainfall statistics, show less inter-model spread, and have absolute and relative humidity dependencies more consistent with observations. Recent work using CPMs also found that rainfall patterns could change with warming, giving rise to disproportionately larger increases in local extremes (Lenderink et al., in prep). At a larger, synoptic scale, a dynamic contribution associated with increasing ascent due to increased latent heating can exhibit super-CC scaling precipitation events (Nie et al., 2018; Lenderink et al., 2017). However, we do not have CPM model runs with sufficient length or ensemble size at hand to perform a rapid attribution study. Therefore, to summarise, our arguments for using relatively coarse resolution (25 km to 50 km) models in this study of convective precipitation events are:

- This event was synoptically driven, with rainfall over a large region and ample moisture available
- We are analysing large-scale multi-day accumulations, rather than digging into the localised rates or organisational structures
- These models account for topography and coastlines reasonably well (compared to GCMs), and this event occurred in a topographically simple region (inland, wide low-lying Mississippi valley)
- We still evaluate the models against observations in the usual way – spatial patterns, seasonal cycles and parameters of the fitted statistical models (Section 2.3)

We conclude that although the models described above do not give us the full picture of this event in terms of spatial distribution of rainfall, and in particular what occurred at local scales, it is the best we have and results are still informative. Since results are analysed for the larger region and 4-day time scale, we are confident we can use the results to indicate the changes in similar large-scale events.

2.1.3 Statistical methods

Methods for observational and model analysis and for model evaluation and synthesis are used according to the World Weather Attribution Protocol, described in Philip et al., (2020), with supporting details found in van Oldenborgh et al., (2021), Ciavarella et al., (2021), Otto et al., (2024) and here. The key steps, presented in Sections 3-6, are: (3) trend estimation from observations; (4) model validation; (5) multi-method multi-model attribution; and (6) synthesis of the attribution statement.

In this section we analyse time series of March-May maximum 4-day accumulated rainfall (rx4day) averaged over the Central Mississippi study region (86-93°W, 34-39°N), as shown in Fig. 1.1.

A nonstationary generalised extreme value (GEV) distribution is used to model this variable. For precipitation, the distribution is assumed to scale exponentially with the covariates, with the dispersion (the ratio between the standard deviation and the mean) remaining constant over time. This formulation reflects the Clausius-Clapeyron (CC) relation, which implies that precipitation scales exponentially with temperature (Trenberth et.al., 2003, O'Gorman and Schneider 2009). The parameters of the statistical model are estimated using maximum likelihood. Results for the AM2 and FLOR models are being synthesised into single model results before inputting into the overall synthesis routine, see Sect 4.1 for details.

For each time series we calculate the return period and intensity of the event under study for the 2024 GMST and for 1.3°C cooler GMST: this allows us to compare the climate of now and of the preindustrial past (1850-1900, based on the Global Warming Index) by calculating the probability ratio (PR; the factor-change in the event's probability) and change in intensity of the event. We also extend this analysis into the future by assessing the influence of a further 1.3°C of global warming from present. This is in line with the latest Emissions Gap Report from the United Nations Environment Programme, which shows that the world is on track for at least 2.6°C temperature rise given currently implemented policies (UNEP, 2024).

2.2 Observational analysis: return period and trend

2.2.1 Analysis of point station data and gridded data

The 4-day accumulated rainfall event had a very large spatial footprint across a swathe of the southern Midwest and central US, particularly the central Mississippi valley (Figs. 1.1 & 2.1). Across the study region, the observed rainfall total is a rare event in the present climate, estimated to occur once every 90-240 years across different observational and reanalysis datasets (Table 2.1). At individual weather station locations across this region, the localised rainfall totals were not as rare, with return period best estimates ranging from 1.5-36 years (Table 2.2), suggesting that the spatial extent of this event was at a major aspect of its severity (though locations without a weather station or which we did not analyse may have experienced more extreme conditions). To study changes in similar large-scale extremes in the climate models we use the 1 in 100 year rx4day event, as this lies within the best estimate range for gridded products and is a useful benchmark for risk analysis more broadly.

In all gridded observational and reanalysis datasets, the fitted statistical model is consistent with the slightly above linear trend with time, with minor deviations in MSWEP, the shortest time series (Fig. 2.2). In each of these datasets, compared to a 1.3°C cooler preindustrial world, the current warming level resulted in an increase in rx4day (Table 2.1, Figs. 2.2 & 2.3). The best estimates for the change in likelihood for the 2025 event associated with this warming range between 2-5, and the change in intensity for an event of equivalent rarity is 13-26% (Table 2.1), exceeding CC scaling. The highest estimated change comes from ERA5, which is statistically significant at the 95% level and shows a change in likelihood of a factor of 5 (1.07 to 10^{10}) and in intensity by 26% (1.3 to 69.7%).

We also tested the sensitivity of these results to the choice of region and at individual locations within the region. Four of the five local weather stations give increases in rx4day with warming, associated with comparable changes in likelihood as those shown by the gridded datasets (best estimates ~2-4), and higher changes in magnitude (best estimates ~22-36%), suggesting super-CC scaling of local extremes (Table 2.2). The station showing a reduction in such extremes, Guntersville, is located at the southeastern corner of the study region, which may be located within a different climatological regime. Across the other two regions (Fig. 2.1, Tables A.1 & A.2), the trend results are largely consistent - all datasets continue to show an increasing trend except CPC for the wider region. However, for this region the uncertainty range in the probability ratio is also substantially larger, by about two orders of magnitude. We are therefore confident that our results are robust to the choice of study region.

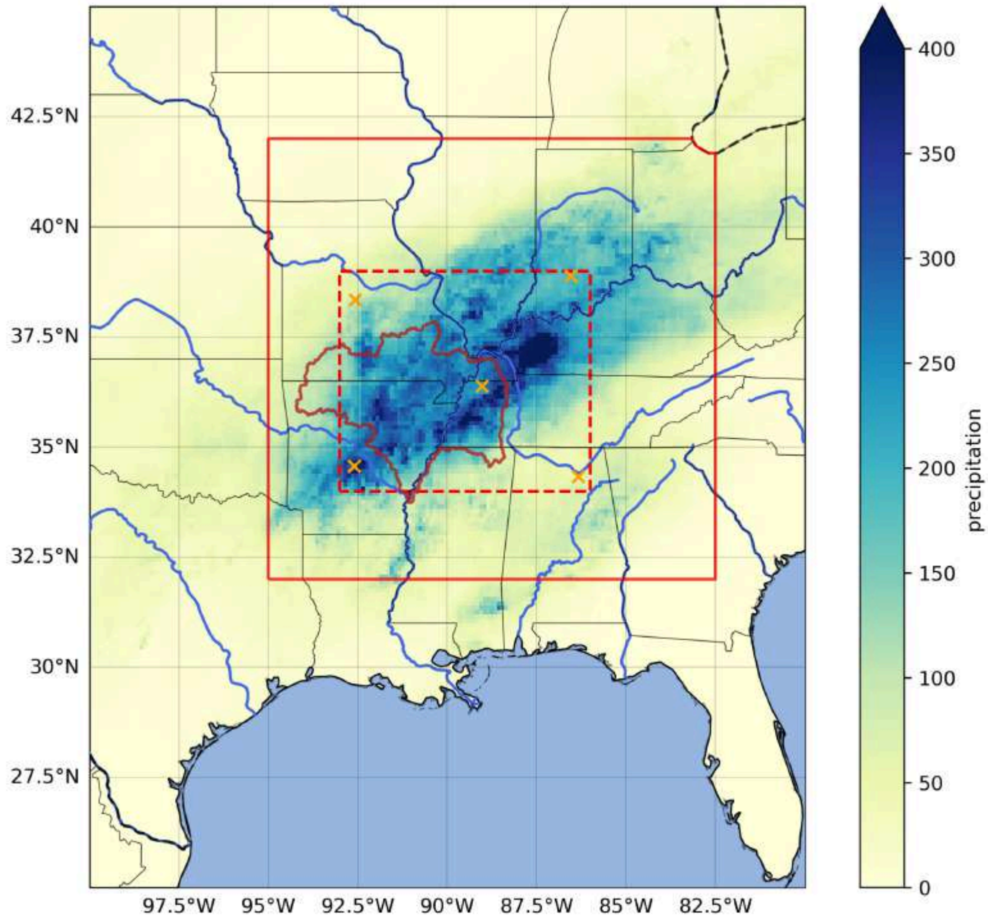

Figure 2.1: *Accumulated precipitation from 3rd-6th April 2025, as in Fig. 1.1, showing the regions and weather stations used to test the sensitivity of the observation-based results to the event definition. The dashed red line shows the final region used here, with trend results for each dataset reported below for this region and the individual weather stations (orange crosses). Results for the larger box highlighted in bright red and sub-catchment of the Mississippi river shown in dark red are given in the appendix.*

Dataset	Event (rx4day)		Trend with GMST	
	Magnitude (mm)	Return period (95% C.I.)	Probability Ratio	Change in magnitude (%)
MSWEP	208.45	220.33 (26.86 - inf)	2.44 (0.45 - 663.95)	22.54 (-12.46 - 79.63)
CPC	178.51	239.93 (41.93 - 46300)	2.03 (0.24 - 12.15)	13.61 (-10.09 - 46.81)
ERA5	146.18	160.31 (33.71 - 10^6)	**4.96 (1.07 - 10^{10})**	**26.30 (1.30 - 69.71)**
Climgrid	159.26	92.19	2.24	15.97

		(25.76 - 16560)	(0.34 - 16.05)	(-13.10 - 50.13)

Table 2.1: *Change in probability ratio and magnitude for rx4day in the central US region due to GMST. Light blue indicates an increasing trend that crosses no change, while dark blue indicates a statistically significant increasing trend. Statistically significant trends are also highlighted in* ***bold*** *font.*

Weather station	Event (rx4day)		Trend with GMST	
	Magnitude (mm)	Return period (95% C.I.)	Probability Ratio	Change in magnitude (%)
Guntersville	112.00	8.01 (3.94 - 37.36)	0.47 (0.07 - 1.46)	-18.33 (-44.32 - 11.19)
Benton	255.30	36.03 (12.93 - 300.56)	2.78 (0.47 - 45.03)	22.54 (-13.83 - 70.98)
Oolitic Purdue	165.20	18.81 (7.85 - 78.20)	2.81 (0.91 - 42.07)	25.28 (-1.40 - 69.56)
Eldon	72.90	1.51 (1.22 - 2.14)	1.71 (0.998 - 2.92)	36.17 (-0.11 - 85.31)
Union City	173.29	20	3.89 (0.89 - 15.86)	23.53 (-1.68 - 53.07)

Table 2.2: *Change in probability ratio and magnitude for rx4day in weather stations in the central US region due to GMST. Light blue (orange) indicates an increasing (decreasing) trend that crosses no change.*

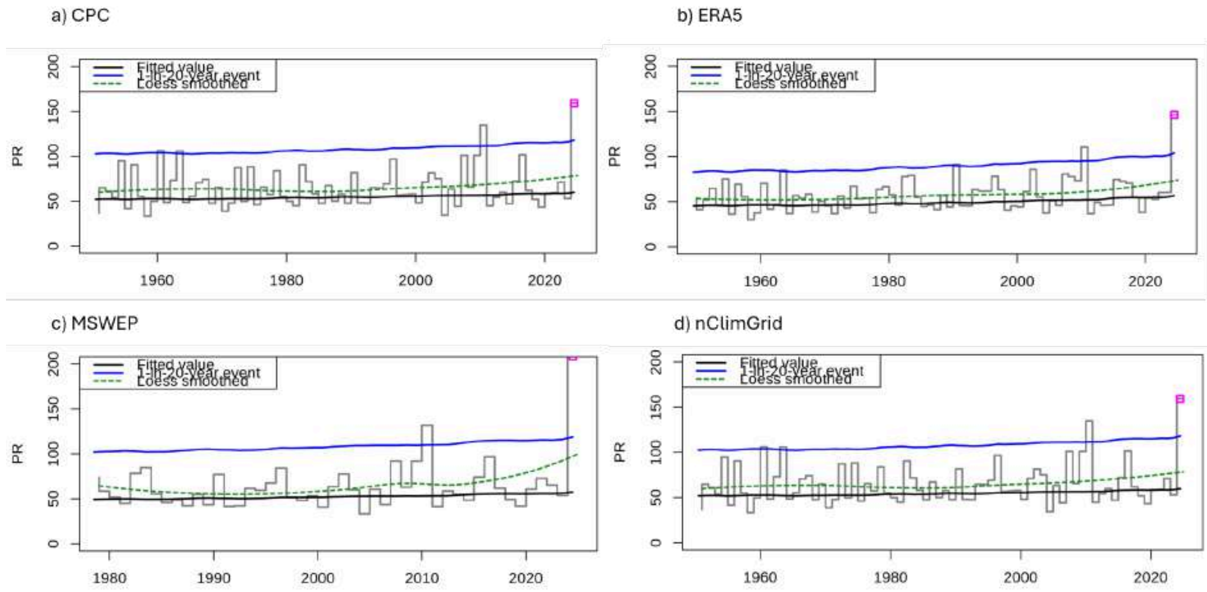

Figure 2.2: *Time series to rx4day in the study region, in CPC, ERA5, MSWEP and nClimGrid. The influence of GMST is shown with the black line on the trend plots, and the green dashed line is a LOESS smoothed trend. The magnitude of the 2025 event is highlighted with a purple box.*

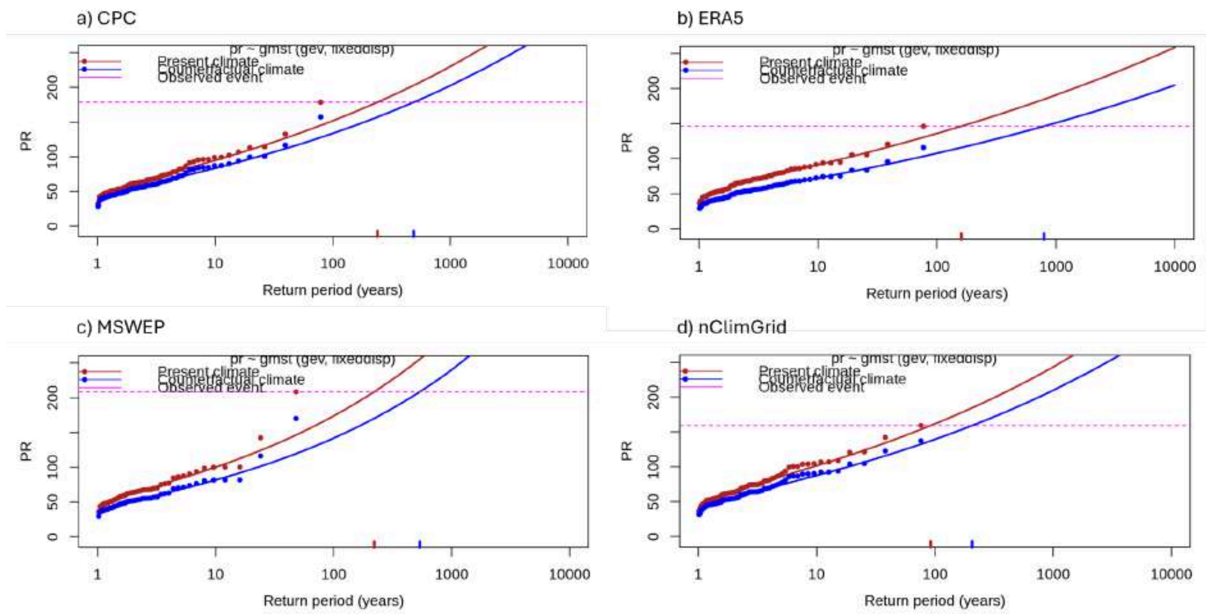

Figure 2.3: *Statistical fits to rx4day in the study region, in CPC, ERA5, MSWEP and nClimGrid. The influence of GMST is shown with the red vs blue probability curves. The magnitude of the 2025 event is highlighted with a purple line.*

2.2.2 Circulation Analogues

Data and methods

Atmospheric flow analogues can be used to assess changes in the intensity of dynamically similar events or changes in the frequency of occurrence of particular circulation patterns (Cattiaux et al., 2010; Vautard et al., 2016; Jézéquel et al., 2018, Thompson et al 2024). Here we use ERA5 data to assess analogues identified from mean sea level pressure (MSLP) since 1950, to detect trends in the frequency of circulation patterns similar to those associated with the heavy rainfall event.

To identify the most similar events, we compute the Euclidean distance between the MSLP anomaly field of the 5th April 2025 and every other day within MAM (1950–2023) over the region bounded by [-110° to -60°E, 20° to 45°N]. To avoid double-counting persistent events, the identified events must be separated by at least 5 days.

We identify the closest 28 analogues across two periods: an early period (1951-1980), defined by weaker climate change signal and a later period (1991-2020), characterised by a stronger climate change signal. This corresponds to the closest 1% of days in each period. The average weather conditions associated with the two sets of analogues - called ‘composites’ - are then compared to assess differences between the two periods We also assess the change in frequency of the closest analogues through time. This is assessed at three different thresholds - the upper 5% of days, upper 10%, and upper 20%. Differences in modes of internal variability between the two time periods can also induce differences in the weather conditions, therefore we cannot identify the role of climate change solely by comparing analogue sets in reanalyses.

Results

The atmospheric conditions observed on the 5th April 2025, depicted in Fig. 1.5, strengthened the Southerly flow near the surface. We show how events similar to this atmospheric level flow have changed in the present (1991–2020) compared to the past (1951–1980). There is a deepening of the low pressure system in the centre, however, this change is not statistically significant (Fig. 2.4 d). In general, the past and present analogues produce rainfall over large parts of the US (Fig. 2.4 f-g). The difference between the two precipitation composites does not show a significant change in rainfall between both periods (Fig. 2.4 h). We note that not all the analogues that occurred produced rainfall in the region or elsewhere (Fig. A3-A4). This means that the analogous circulation patterns alone are not a good predictor of rainfall, or that the set of selected parameters (MSLP, one-day average) is not optimal to characterize these event types. The warm temperature (Fig. 2.4 i) also led to high moisture content in the air masses (Section 3). The inflow of moist air from the Gulf of Mexico is also confirmed by the back-trajectories (Fig. 1.4). We also assess the change in annual frequency of the most similar events (Fig. 2.5). In the most similar 5% and 10% of events there is no detectable trend through time. Our results imply that climate change did not alter atmospheric circulations, but caution that this result is contingent on the variables and parameters selected here and should be explored further.

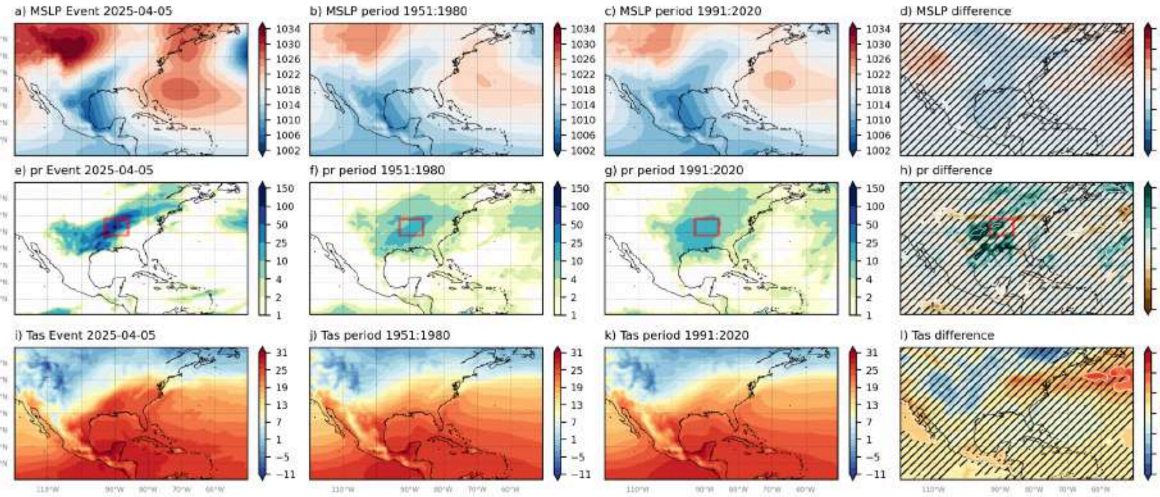

Figure 2.4: *Changes in atmospheric analogues. (a) MSLP (hPa) for the event, 5 Apr 2025. b) Composite of the top 28 analogue days from the past period, 1951-1980. c) Composite of the top 28 analogue days from the present period, 1991-2020. d) Difference between the composites of past and present (present minus past). e-h) as in a-d for the rainfall field (mm). i-l) as in a-d for the 2m temperature field (°C). MLSP used to identify analogues in all plots. Hashing signifies regions where the signal is not significant based on a two-sided t-test.*

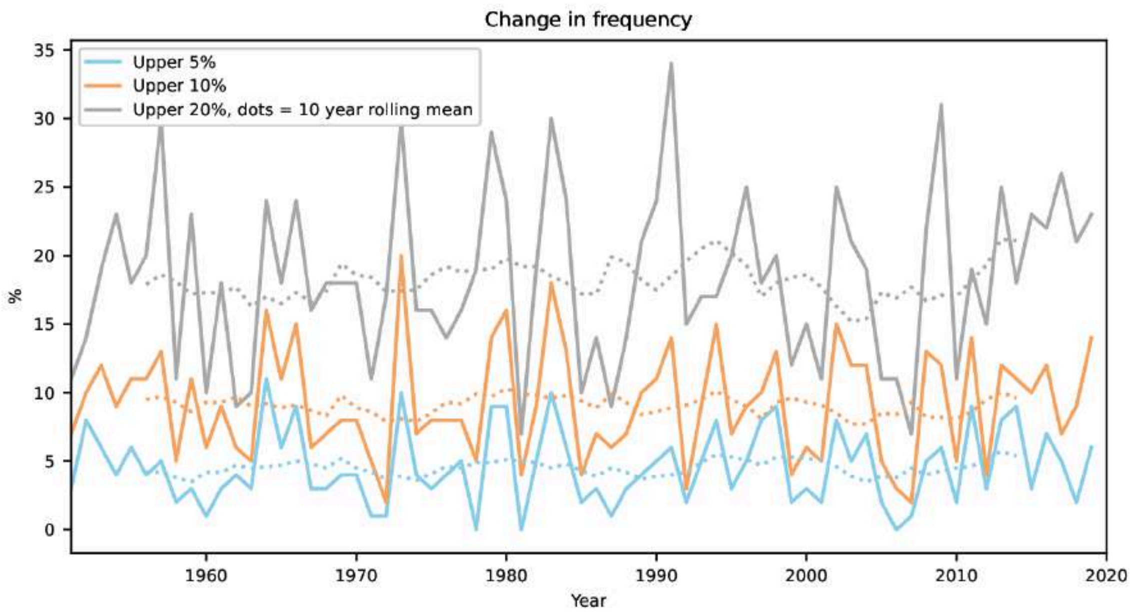

Figure 2.5: *Trends in frequency of the most similar events. Number of "good" analogues per year (in MAM) at three threshold levels: the closest 5%, 10% and 20% of most similar days (based on Euclidean distance of MSLP field. Multiannual trends (dotted lines) are plotted.*

2.3 Model evaluation

In the subsections below we show the results of the model evaluation for each location. The climate models are evaluated against the observations in their ability to capture:

1. Seasonal cycles: For this, we qualitatively compare the seasonal cycles based on model outputs against observations-based cycles. We discard the models that exhibit ill-defined peaks in their seasonal cycles.

2. Spatial patterns: Models that do not match the observations in terms of the large-scale precipitation patterns are excluded.

3. Parameters of the fitted statistical models. We discard the model if the model and observation parameters ranges do not overlap.

The models are labelled as 'good','reasonable', or 'bad' based on their performances in terms of the three criteria discussed above. A model is given an overall rating of 'good' if it is rated 'good' for all three characteristics. If there is at least one 'reasonable', then its overall rating will be 'reasonable' and 'bad' if there is at least one 'bad'. For each framing or model setup we also use models that only just pass the evaluation tests if we only have five models or less for that framing that perform well.

Observations / models	**Seasonal cycle**	**Spatial pattern**	**Dispersion parameter**	**Shape parameter**	**Overall**	**Keep?**
CPC			0.266 (0.191, 0.308)	0.144 (-0.035, 0.46)		
ERA5			0.243 (0.195, 0.282)	0.094 (-0.152, 0.304)		
MSWEP			0.256 (0.183, 0.316)	0.218 (-0.09, 0.741)		
ClimGrid			0.266 (0.205, 0.311)	0.139 (-0.056, 0.359)		
CAM-MPAS-HR	good	good	0.302 (0.213, 0.371)	0.061 (-0.356, 0.426)	good	y
CAM-MPAS-LR	good	reasonable	0.277 (0.194, 0.331)	-0.241 (-0.535, 0.015)	reasonable	y
CMCC-CM2-HR4	good	reasonable	0.237 (0.148, 0.292)	-0.015 (-0.294, 0.512)	reasonable	y
CMCC-CM2-VHR4	good	reasonable	0.252 (0.172, 0.309)	-0.058 (-0.477, 0.33)	reasonable	y
FGOALS-f3-H	bad	bad	0.262 (0.144, 0.307)	-0.328 (-0.72, 0.592)	reasonable	n
HadGEM3-GC31-HM	good	good	0.268 (0.209, 0.315)	-0.249 (-0.788, 0.026)	reasonable	y
HadGEM3-GC31-LM	good	good	0.231 (0.159, 0.272)	0.171 (-0.035, 0.567)	good	y
HadGEM3-GC31-MM	good	good	0.279 (0.209, 0.33)	0.064 (-0.299, 0.413)	good	y
HiRAM-SIT-HR	good	good	0.275 (0.215, 0.324)	-0.099 (-0.587, 0.111)	good	y
HiRAM-SIT-LR	reasonable	reasonable	0.238 (0.184, 0.28)	-0.041 (-0.331, 0.261)	reasonable	y
MPI-ESM1-2-HR	reasonable	reasonable	0.312 (0.22, 0.381)	-0.38 (-0.706, -0.004)	reasonable	y
MPI-ESM1-2-XR	reasonable	reasonable	0.265 (0.181, 0.33)	-0.211 (-0.715, 0.307)	reasonable	y
NICAM16-7S	reasonable	reasonable	0.279 (0.21, 0.346)	0.119 (-0.427, 0.525)	reasonable	y
NICAM16-8S	reasonable	reasonable	0.303 (0.229, 0.352)	-0.032 (-0.311, 0.223)	reasonable	y

Observations / models	Seasonal cycle	Spatial pattern	Dispersion parameter	Shape parameter	Overall	Keep?
CanESM2_CanRCM4	good	good	0.246 (0.183, 0.293)	-0.246 (-0.643, 0.126)	reasonable	y
CanESM2_CRCM5-OUR	good	good	0.209 (0.16, 0.258)	-0.006 (-0.362, 0.318)	good	y
CanESM2_CRCM5-UQAM	good	reasonable	0.222 (0.17, 0.261)	0.114 (-0.256, 0.405)	reasonable	y
CNRM-CM5_CRCM5-OUR	good	reasonable	0.272 (0.213, 0.316)	-0.203 (-0.65, -0.052)	reasonable	y
GFDL-ESM2M_CRCM5-OUR	good	reasonable	0.241 (0.178, 0.286)	0.031 (-0.307, 0.346)	reasonable	y
GFDL-ESM2M_WRF	reasonable	reasonable	0.227 (0.16, 0.271)	-0.094 (-0.448, 0.143)	reasonable	y
HadGEM2-ES_REMO2015	good	reasonable	0.211 (0.156, 0.253)	0.035 (-0.262, 0.323)	reasonable	y
HadGEM2-ES_WRF	good	reasonable	0.198 (0.154, 0.241)	-0.009 (-0.543, 0.31)	reasonable	y
MPI-ESM-LR_CRCM5-OUR	good	reasonable	0.205 (0.153, 0.243)	-0.129 (-0.445, 0.08)	reasonable	y
MPI-ESM-LR_CRCM5-UQAM	good	reasonable	0.242 (0.178, 0.284)	-0.088 (-0.363, 0.095)	reasonable	y
MPI-ESM-LR_REMO2015	good	good	0.299 (0.229, 0.357)	0.077 (-0.255, 0.345)	good	y
MPI-ESM-LR_WRF	reasonable	reasonable	0.236 (0.184, 0.274)	-0.093 (-0.502, 0.092)	reasonable	y
MPI-ESM-MR_CRCM5-UQAM	good	reasonable	0.209 (0.164, 0.249)	0.025 (-0.228, 0.287)	reasonable	y
NorESM1-M_REMO2015	good	good	0.175 (0.131, 0.205)	0.071 (-0.222, 0.404)	reasonable	y
AM2.5C360						
Ensemble member 6	good	reasonable	0.249 (0.184, 0.304)	0.158 (-0.251, 0.424)	reasonable	Y (ens)
Ensemble member 7	good	reasonable	0.195 (0.149, 0.227)	-0.097 (-0.435, 0.119)	reasonable	Y (ens)
Ensemble member 8	good	reasonable	0.278 (0.211, 0.335)	-0.333 (-0.689, -0.138)	reasonable	Y (ens)
FLOR						
Ensemble member 1	reasonable	good	0.27 (0.183, 0.32)	-0.017 (-0.404, 0.339)	reasonable	Y (ens)
Ensemble member 2	reasonable	good	0.242 (0.152, 0.288)	0.095 (-0.155, 0.599)	reasonable	Y (ens)
Ensemble member 3	reasonable	good	0.235 (0.174, 0.278)	-0.222 (-0.493, -0.016)	reasonable	Y (ens)
Ensemble member 4	reasonable	good	0.287 (0.21, 0.337)	-0.136 (-0.452, 0.053)	reasonable	Y (ens)
Ensemble member 5	reasonable	good	0.218 (0.138, 0.266)	-0.126 (-0.381, 0.255)	reasonable	Y (ens)
Ensemble member 6	reasonable	good	0.185 (0.133, 0.22)	0.035 (-0.188, 0.303)	reasonable	Y (ens)
Ensemble member 7	reasonable	good	0.21 (0.152, 0.25)	-0.15 (-0.512, 0.08)	reasonable	Y (ens)
Ensemble member 8	reasonable	good	0.22 (0.169, 0.263)	-0.084 (-0.388, 0.11)	reasonable	Y (ens)
Ensemble member 9	reasonable	good	0.277 (0.213, 0.322)	-0.306 (-0.684, -0.072)	reasonable	Y (ens)
Ensemble member 10	reasonable	good	0.303 (0.229, 0.356)	-0.134 (-0.421, 0.081)	reasonable	Y (ens)

Table 2.3: *Evaluation results of the climate models considered for attribution analysis of rx4day. For each model, the best estimates of the Dispersion and Shape parameters are shown, along with 95% confidence intervals in parentheses. Furthermore evaluation of the seasonal cycle and spatial pattern are shown.*

2.4 Multi-method multi-model attribution

This section shows the probability ratios and change in intensity for models that passed model evaluation and also includes the values calculated from the fits with observations. The values for the AM2 and FLOR ensembles have already been synthesised into a single result value for both the Probability Ratio and the change in intensity.

Observations / models	**100-year event (mm)**	**(a) -1.3C vs present**		**(b) Present vs +1.3C**	
		Probability ratio	**Change in intensity (%)**	**Probability ratio**	**Change in intensity (%)**
CPC	179	2.03 (0.242, 12.2)	13.6 (-10.1, 46.8)		
ERA5	146	4.96 (1.07, 1.74e+10)	26.3 (1.27, 69.7)		
MSWEP	208	2.44 (0.45, 664)	22.5 (-12.5, 79.6)		
ClimGrid	159	2.24 (0.343, 16)	16 (-13.1, 50.1)		
CAM-MPAS-HR	133	0.895 (0.115, 7.27)	-1.59 (-24.6, 28.2)		
CAM-MPAS-LR	114	2.93 (0.133, 63500)	9.29 (-18.5, 45.3)		
CMCC-CM2-HR4	89	0.684 (0.125, 12.7)	-3.7 (-21.9, 20.8)		
CMCC-CM2-VHR4	128	159 (3.2, Inf)	35.7 (13.8, 62)		
HadGEM3-GC31-HM	123	15.6 (0.214, Inf)	14.7 (-13.8, 41.6)		
HadGEM3-GC31-LM	160	1.21 (0.294, 9.02)	3.15 (-18.6, 28.7)		
HadGEM3-GC31-MM	127	0.68 (0.0947, Inf)	-4.08 (-29.1, 36.2)		
HiRAM-SIT-HR	126	0.852 (0.126, Inf)	-1.38 (-19.2, 21.9)		
HiRAM-SIT-LR	143	6.85 (0.725, 485000)	18.8 (-2.23, 45.1)		
MPI-ESM1-2-HR	74	0.0684 (0.0206, 1.13)	-17.8 (-33, 0.631)		
MPI-ESM1-2-XR	93	13.7 (0.241, Inf)	10.5 (-11, 31.8)		
NICAM16-7S	128	1.32 (0.204, 14.9)	3.08 (-15.3, 26.6)		
NICAM16-8S	138	9.08 (0.749, 366000)	24.1 (-3.61, 56.1)		
CanESM2_CanRCM4	117	1.77 (0.298, 16.1)	4.44 (-8.34, 17.8)	3 (1.69, 5.93)	8.17 (3.52, 12.5)
CanESM2_CRCM5-OUR	105	0.868 (0.112, 9.08)	-1.01 (-14.5, 15.1)	2.44 (1.46, 4.51)	8.24 (3.04, 13)

Observations / models	100-year event (mm)	(a) -1.3C vs present		(b) Present vs +1.3C	
		Probability ratio	Change in intensity (%)	Probability ratio	Change in intensity (%)
CanESM2_CRCM5-UQAM	130	2.15 (0.727, 64.5)	9.01 (-3.25, 22.8)	2.18 (1.43, 3.98)	8.41 (4.16, 12.6)
CNRM-CM5_CRCM5-OUR	91	0.405 (0.0219, 9.22)	-5.58 (-24.5, 11)	2.62 (0.966, 6.97)	6.63 (-0.243, 13)
GFDL-ESM2M_CRCM5-OUR	99	0.626 (0.107, 3.56)	-5.01 (-21.9, 13.2)	2.29 (1.12, 5.38)	9.18 (1.49, 16.6)
GFDL-ESM2M_WRF	94	2.66 (0.145, Inf)	6.46 (-11.7, 25.7)	3.61 (1.7, 9.41)	10.3 (4.68, 15.6)
HadGEM2-ES_REMO2015	117	1.69 (0.209, 61.8)	4.83 (-12.6, 26.8)	3.02 (1.63, 7.68)	8.77 (3.93, 13.6)
HadGEM2-ES_WRF	99	1.07 (0.0642, 6.48)	0.507 (-15.6, 15.3)	1.75 (1.06, 2.85)	5.3 (0.528, 9.16)
MPI-ESM-LR_CRCM5-OUR	111	1.98 (0.237, 45.5)	5.98 (-11.1, 24.1)	1.7 (1.04, 2.92)	6.27 (0.363, 12)
MPI-ESM-LR_CRCM5-UQAM	112	0.853 (0.189, 7.21)	-1.42 (-15.8, 16.2)	1.83 (1.09, 3.09)	5.75 (0.69, 10.5)
MPI-ESM-LR_REMO2015	160	4.2 (0.791, Inf)	23.8 (-6.19, 62)	1.42 (0.543, 3.23)	4.14 (-5.45, 12.3)
MPI-ESM-LR_WRF	101	1.2 (0.247, 164)	1.38 (-13.3, 16.3)	1.32 (0.683, 2.69)	2.05 (-2.5, 6.59)
MPI-ESM-MR_CRCM5-UQAM	120	9.97 (0.995, Inf)	17.1 (-0.04, 38.3)	3.18 (1.83, 5.63)	10.8 (5.44, 15.7)
NorESM1-M_REMO2015	90	0.883 (0.191, 41.5)	-1.37 (-17.7, 21.3)	2.09 (1.07, 5.16)	5.56 (0.462, 11.1)
AM2.5C360 ensemble (3 members)	105	1.73 (0.225, 293)	5.56 (-12.4, 26.3)	3.6 (1.43, 8.25)	11.5 (3.3, 18.9)
FLOR ensemble (10 members)	102	2.1 (0.59, 29.3)	7.32 (-4.92, 21.2)	2.03 (0.932, 4.52)	6.55 (-1.16, 14.1)

Table 2.4: *Event magnitude, probability ratio and change in intensity for 100-year return period for rx4day for observational datasets and each model that passed the evaluation tests. (a) from pre-industrial climate to the present (that is, after 1.3℃ of warming) and (b) from the present to 2.6℃ above pre-industrial climate (that is, after a further 1.3℃ of warming).*

2.5 Hazard synthesis

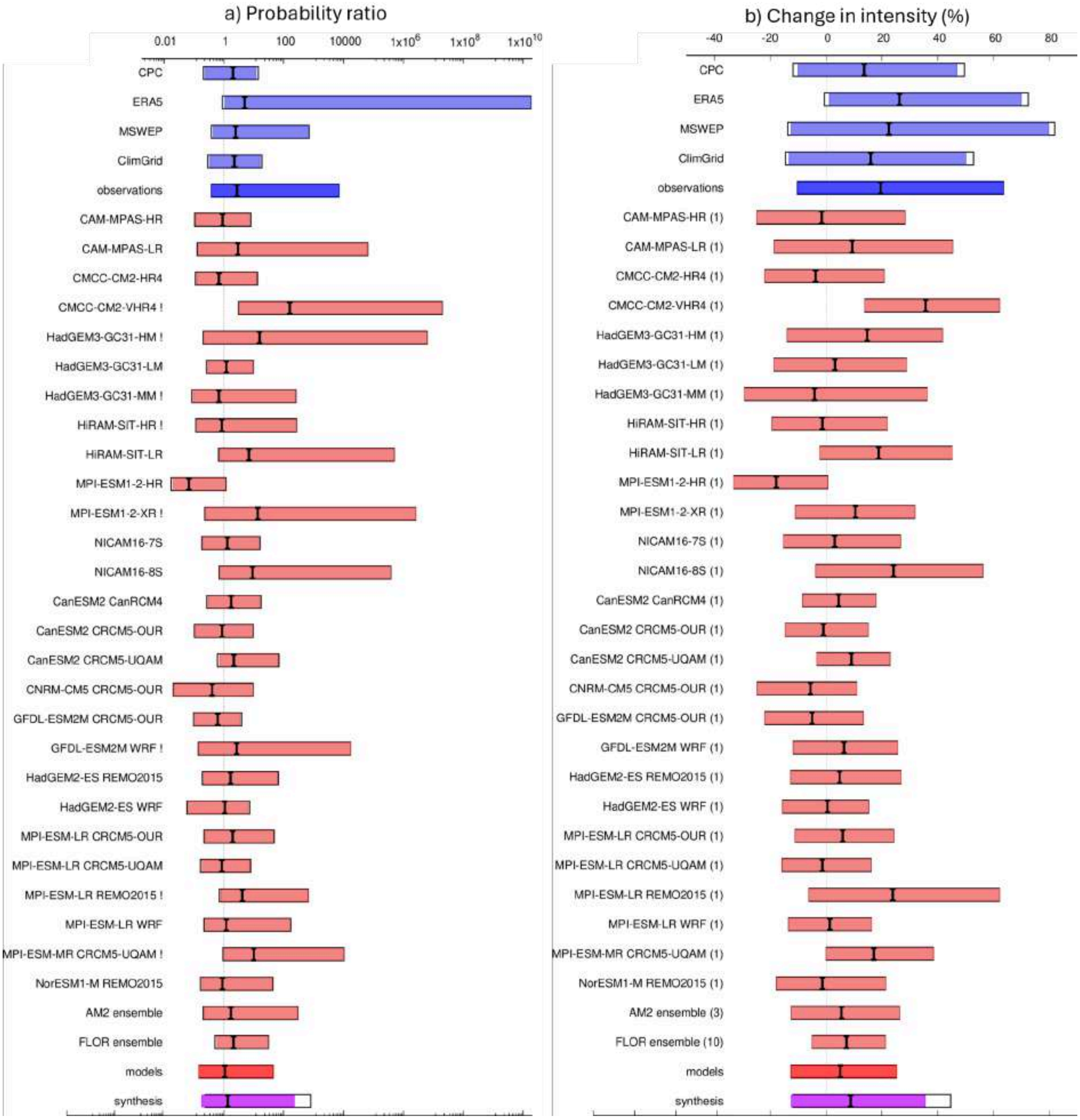

Figure 2.4: *Synthesised changes for a 100-year 4-day MAM maximum rainfall event over the study region domain due to GMST. Changes in PR (left) and intensity (right) are shown for a historical period comparing the past 1.3°C cooler climate with the present. Note: AM2 refers to the AM2.5C360 ensemble described in Section 2.1.2.*

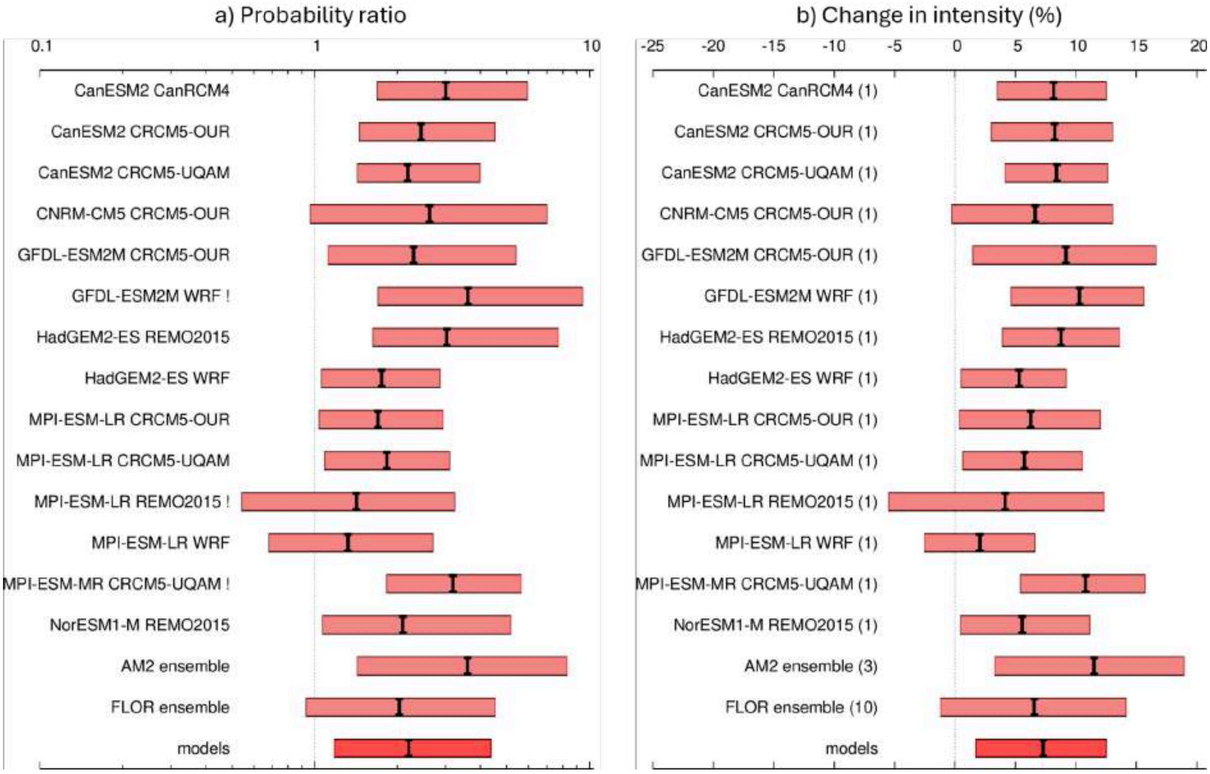

Figure 2.5: *Synthesised changes for a 100-year 4-day MAM maximum rainfall event over the study region domain due to GMST. Changes in PR (left) and intensity (right) are shown for a future period comparing the future 1.3°C warmer climate with the present. Note: AM2 refers to the AM2.5C360 ensemble described in Section 2.1.2.*

For the rx4day event definition described above we evaluate the influence of anthropogenic climate change by calculating the probability ratio as well as the change in intensity, using a combination of observations/reanalyses and climate models. Models which do not pass the evaluation described above are excluded from the analysis. The aim is to synthesise results from models that pass the evaluation along with the observations-based products, to give an overarching attribution statement.

Figures 2.4 & 2.5 show the changes in probability and intensity for the observations (blue) and models (red). Before combining them into a synthesised assessment, first, a representation error is added (in quadrature) to the observations, to account for the difference between observations-based datasets that cannot be explained by natural variability. This is shown in these figures as white boxes around the light blue bars. The dark blue bar shows the average over the observation-based products. Next, a term to account for intermodel spread is added (in quadrature) to the natural variability of the models. This is shown in the figures as white boxes around the light red bars. The dark red bar shows the model average, consisting of a weighted mean using the (uncorrelated) uncertainties due to natural variability plus the term representing intermodel spread (i.e., the inverse square of the white bars). In the model average, the results of the AM2 and FLOR models are combined to one single model result for each of them first, and this is synthesised together with all other model results

Observation-based products and models are combined into a single result in two ways. Firstly, we neglect common model uncertainties beyond the intermodel spread that is depicted by the model average, and compute the weighted average of models (dark red bar) and observations (dark blue bar): this is indicated by the magenta bar. As, due to common model uncertainties, model uncertainty can be larger than the intermodel spread, secondly, we also show the more conservative estimate of an unweighted, direct average of observations (dark blue bar) and models (dark red bar) contributing

50% each, indicated by the white box around the magenta bar in the synthesis figures.

Data		Attributable trends due to GMST	
		Probability ratio (95% CI)	**Intensity change (%) (95% CI)**
Observations	**Past-Present**	2.72 (0.38 - 7170)	19.5 (-10.3 - 63.4)
Models		1.08 (0.15 - 44.4)	5.08 (-12.5 - 25.3)
Synthesis		1.36 (0.19 - 222)	8.72 (-12.4 - 35.6)
Models only	**Present-Future**	**2.20** **(1.18 - 4.37)**	**7.30** **(1.76 - 12.5)**

Table 2.5: *Summary of results for rx4day, presented in Figs 2.4 & 2.5: changes due to GMST include past-present changes and present-future changes. Statistically significant increases in probability and intensity are highlighted in dark blue, while non-significant increases are highlighted in light blue. Statistically significant changes are also highlighted in* ***bold*** *font.*

The results for rx4day generally indicate increasing intensity and likelihood with increasing GMST (Table 2.5). The observational datasets estimate that events like in early April 2025 have become 2.7 (0.4 to 7200) times as likely and, equivalently, 20% (-10 to 64%) more intense. The combined model estimates suggest only a very slight increase, commensurate with no change, with an increase in likelihood by a factor of 1.08 (0.15 to 44) and intensity by 5.1% (-12.5 to 25%). When synthesised, the overall result is highly uncertain, with an increase in likelihood by a factor of 1.36 (0.19 to 222) and intensity by 8.7% (-12.4 to 36%). In the future, a strong signal emerges in model projections, with an increase in likelihood by a factor of 2.2 (1.2 to 4.4) and intensity by 7.3% (1.8 to 12.5%), approximately in line with CC scaling.

3 Sea Surface Temperatures in the Gulf of Mexico

3.1 Data and Methods

Climate Central's Climate Shift Index: Ocean (Ocean CSI) tool is used to rapidly compute the influence of human-caused climate change on Sea Surface Temperatures in the Gulf of Mexico on the days in which moisture was transported (03-04/04, Fig. 1.4). The methodology underpinning this attribution tool is based on peer-reviewed research (Giguere et. al, 2024). It uses a combination of an empirically-driven attribution method using OISST data (Huang et. al, 2021), and model simulations using an ensemble of 13 debiased CMIP6 models. Results from these two methods are aggregated to compute a single metric measuring the increase in likelihood of an SST occurring as a result of climate change. This metric, called the Ocean CSI, is the ratio of the probability of a temperature occurring in today's climate to the probability of that same temperature occurring in a world without human-caused climate change. In addition to likelihood changes, the methods used to compute the Ocean CSI can be used to measure the temperature increase in a location on a given day due to climate change (Giguere et. al, 2024). This allows us to calculate the specific difference between an observed daily temperature in a location and what that temperature would have been in a counterfactual world without climate change. The Ocean CSI uses 0.25° by 0.25° latitude-longitude grid cells. It took roughly 1 - 1.5 days for moist air from the Gulf of Mexico to transport north towards the precipitation event (Section 1.2.1). Thus, we computed the Ocean CSI and the climate-driven ocean warming over the entire region for 03-04/04.

3.2 Attribution Analysis

On average, temperatures over the Gulf or Mexico were made 1.2°C (2.2°F) warmer by human caused climate change. The strongest climate-driven warming was in the northern regions of the Gulf, along the coast of Texas and eastwards towards west Florida (Fig. 3.1). On average, sea surface temperatures over the region were made about 14 times more likely to occur across the two days (Fig. 3.2). These results are the same if the SSTs on the 5th April are included too.

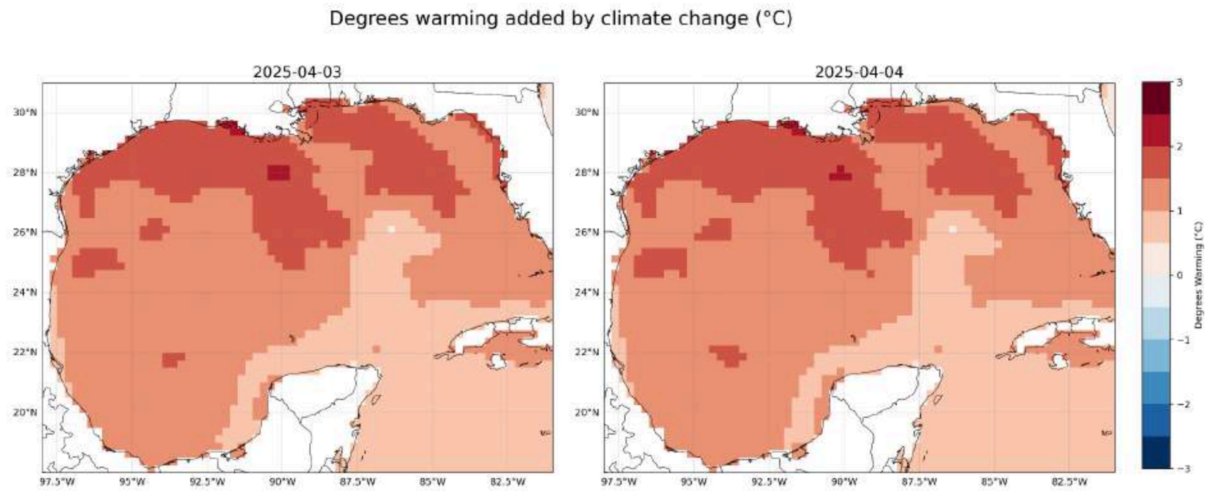

Figure 3.1: *Change in SSTs due to anthropogenic climate change across the Gulf of Mexico on 03/04/2025 and 04/04/2025.*

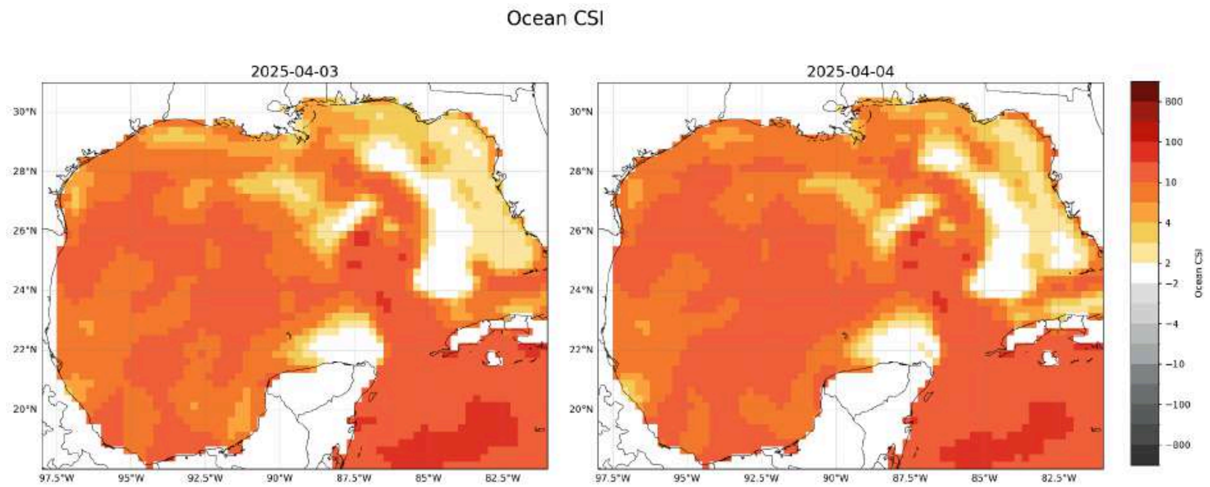

Figure 3.2: *Climate Shift Index of SSTs across the Gulf of Mexico on 03/04/2025 and 04/04/2025, showing the change in likelihood of reaching such temperatures as a result of anthropogenic climate change.*

Warmer air can hold more moisture, and warmer sea surface temperatures (SSTs) contribute to increased evaporation, leading to warmer and more humid ocean air masses, enhancing moisture transport via the low-level atmospheric river. The Ocean CSI shows that SSTs in the Gulf were an estimated 1.2°C warmer than they would have been without climate change. This additional ocean heat allowed for higher atmospheric moisture and contributed to more intense precipitation in the affected region.

4 Hazard discussion and conclusions

There is a major discrepancy between observed trends in the extreme precipitation index and the trends simulated by many of the climate models used here, which show an estimate close to no change when synthesised into a single estimate. This occurs because the range of models disagree on the sign of the change for the historical period; while many individual models show changes similar to the observed trends (with some giving large and statistically significant increases), others show weaker or decreasing trends. Overall, increasing trends (indicated by the best estimates) are found in 8/13 HighResMIP models, 9/14 CORDEX models, and the synthesised FLOR and AM2 ensembles, for a total of 19/29 models (66%). Within the ensembles, 9/10 FLOR runs and 2/3 AM2 runs show increasing trends. The differences in trends at present may be related to the influence of aerosols and their representation in individual models (e.g. as in Wang et al., 2021), but this requires further exploration.

Observed trends in precipitation extremes in this region are also found in other studies using different methods and are assessed as being attributable to climate change by the IPCC AR6 report. Furthermore, it is clear that this rainfall event was fuelled by moisture from the Gulf of Mexico, where very warm waters contributed to higher evaporation rates. These waters were made approximately 1.2°C (2.2°F) hotter by anthropogenic climate change, and such conditions are now 14 times more likely than they were in a 1.3°C cooler world. Additionally, we did not detect a trend in the frequency of circulation analogues, reinforcing the role of amplified thermodynamics, potentially combined with dynamical feedbacks (e.g. Nie et al., 2018), in driving this trend.

Overall, from a combination of observed trends in extreme precipitation (which is consistent with other studies), and the enhanced SSTs leading to greater moisture availability, we conclude that anthropogenic climate change amplified the extreme rainfall in April 2025. The synthesised result gives an increase in likelihood by a factor of 1.36 (0.19 to 222) and intensity by 8.7% (-12.4 to 36%), but this is likely a conservative result due to the large model uncertainties. As a result of these uncertainties, we communicate that the event was made approximately 1.4 times as likely and, equivalently, 9% more intense, but caution that the attributable trends may be as large as observations suggest, having become 2.7 (0.4 to 7200) times as likely and, equivalently, 20% (-10 to 64%) more intense as the world has warmed. The robust anthropogenic increasing trends in Gulf of Mexico SSTs and the resulting rainfall rates are of significant societal relevance. Additionally, while extreme local rainfall rates were not assessed in this study, a substantial literature (Section 1.1) also indicates increases in these phenomena related to climate change.

Finally, in sharp contrast to the past-present assessment, all assessed model projections (CORDEX, AM2 and FLOR) show that such extremes will get worse in a warmer world. Moreover, all models with a negative or small positive trend up to now show a change towards a stronger increase in such extremes as warming continues. In particular, given current climate policies, the likelihood and intensity of large-scale multi day precipitation extremes in this region will become significantly more frequent and intense. In a world 2.6°C warmer than preindustrial times, similar events will be more than twice as likely and about 7% more intense than at present. This strengthens the conclusion above that in some climate models the signal has not yet emerged, so even though we cannot quantify the role of anthropogenic climate change yet (because the variability dominates in some models), it is clear that it is amplifying extreme rainfall.

5 Vulnerability and exposure

Heavy rainfall in the central and southern US associated with the early April storm system covered parts of 8 states, and included the metro areas of Memphis, Tennessee, Huntsville, Alabama, St Louis, Illinois, Springfield, Missouri, Louisville and Frankfort, Kentucky and Little Rock, Arkansas. While a major part of the risk associated with the storm was tornadic activity, the heavy rainfall also resulted in both flash and riverine floods. Over 10-15" of rain ultimately fell in some locations leading to severe flooding in some river basins as well as some mudslides and landslides (NWS, 2025).

The National Weather Service (NWS) forecast office in Paducah, KY covers 58 counties across southern Illinois and Indiana, southeastern Missouri and western Kentucky and reported that **all** of them experienced flash flooding during some point between April 2 and 6 (NWS, 2025). This was followed by moderate to major riverine flooding which came a few days later (April 6 - 15) when rivers crested, including the worst flooding in over 60 years at the Green River in Kentucky (NWS, 2025). The extreme rainfall made roads impassable (including over 500 road closures in Kentucky alone), requiring numerous water rescues, created sinkholes, and inundated homes and businesses (NWS, 2025; KY Governor, 2025). The event also damaged water distribution services (e.g. Frankfort, KY water and wastewater systems were inundated) and disrupted critical government services (KY Governor, 2025).

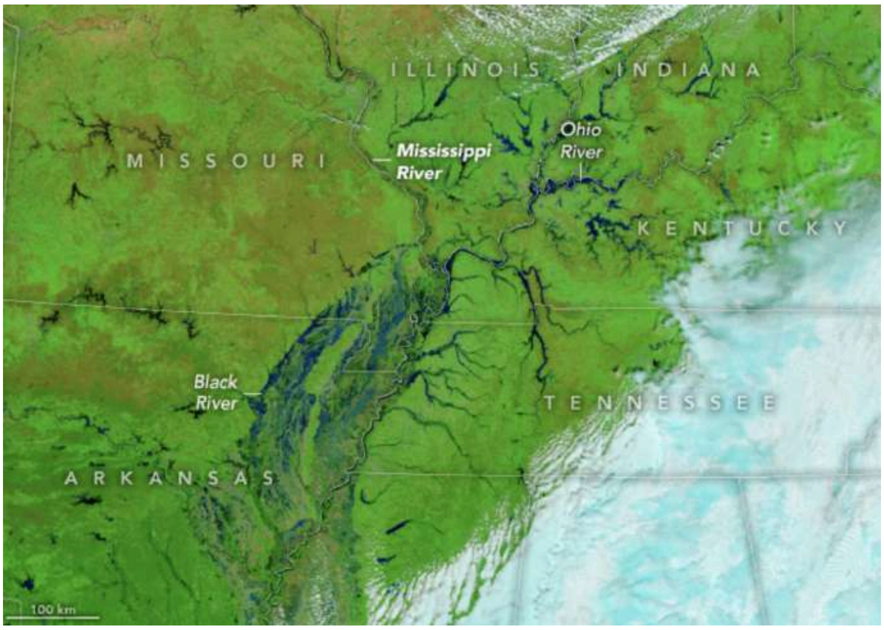

Figure 5.1: NASA VIIRS Satellite showing flooding on April 7th along the Mississippi following days of extreme rainfall. **Source:** NASA Earth Observatory

In this section, we examine the vulnerability and exposure factors that may have played a role in either exacerbating or alleviating the ultimate impacts of this historic event.

Agriculture

From 1941 to 2000, land use in the Mississippi River Basin has changed from majority forest and grassland to agriculture (Rajib et al, 2021). The spring flooding occurred when farmers had already sown seeds for crops such as rice, soybeans, corn and wheat, and added significant inputs like fertilizer. The University of Arkansas estimates the damage to crops to total at least 78 million USD in Arkansas, with rice accounting for 46% of the acres flooded (Arkansas Advocate, 2025). In some places that water has stagnated for days or over a week. Some crops, like soybeans (30% of acres flooded) are still within the optimal planting window and can be replanted, limiting losses, whereas others like winter wheat (accounting for 1% of acres flooded), cannot be replanted now (Arkansas Advocate, 2025). The cost of replating is estimated at 42.04 million USD (Arkansas Advocate, 2025). The US Dept of Agriculture (USDA) is offering disaster assistance to farmers affected by the tornadoes and flooding (USDA, 2025). The timing of the floods, early in spring helped to avoid larger damage, since crops like cotton and peanuts had not been planted yet (TB&P, 2025). As the water continues to move downstream, additional areas may also flood.

Urban planning and informality

The Southern parts of the affected areas have been previously identified as areas of high exposure and high social vulnerability compared to other parts of the US with some of the highest number of hot spots found in the affected areas including in Mississippi, Louisiana and Arkansas along the Mississippi River (Tate et al., 2021; Environmental Defense Fund, 2025 see Fig. 5.2 below). Hotspots of high vulnerability and exposure are usually found in the rural areas and disproportionately affect African Americans and Indigenous populations as well as people living in mobile homes (Tate et al., 2021). Furthermore, results show that income level, education and insurance coverage is particularly low in highly exposed areas (Tate et al., 2021). While higher vulnerabilities might persist in the rural areas, substantial parts of urban areas exhibit exposure to flooding with 16% of the buildings in Memphis being under potential flood risk, 19% in Huntsville, 18% in St. Louis, 9% in Springfield, 22% in Louisville, and 13% in Little Rock (Climate Check, 2025). Within cities inequalities in vulnerability and exposure mostly affect populations residing in low lying areas with lower access to emergency shelter and less adequate infrastructural developments (Emergun et al., 2024).

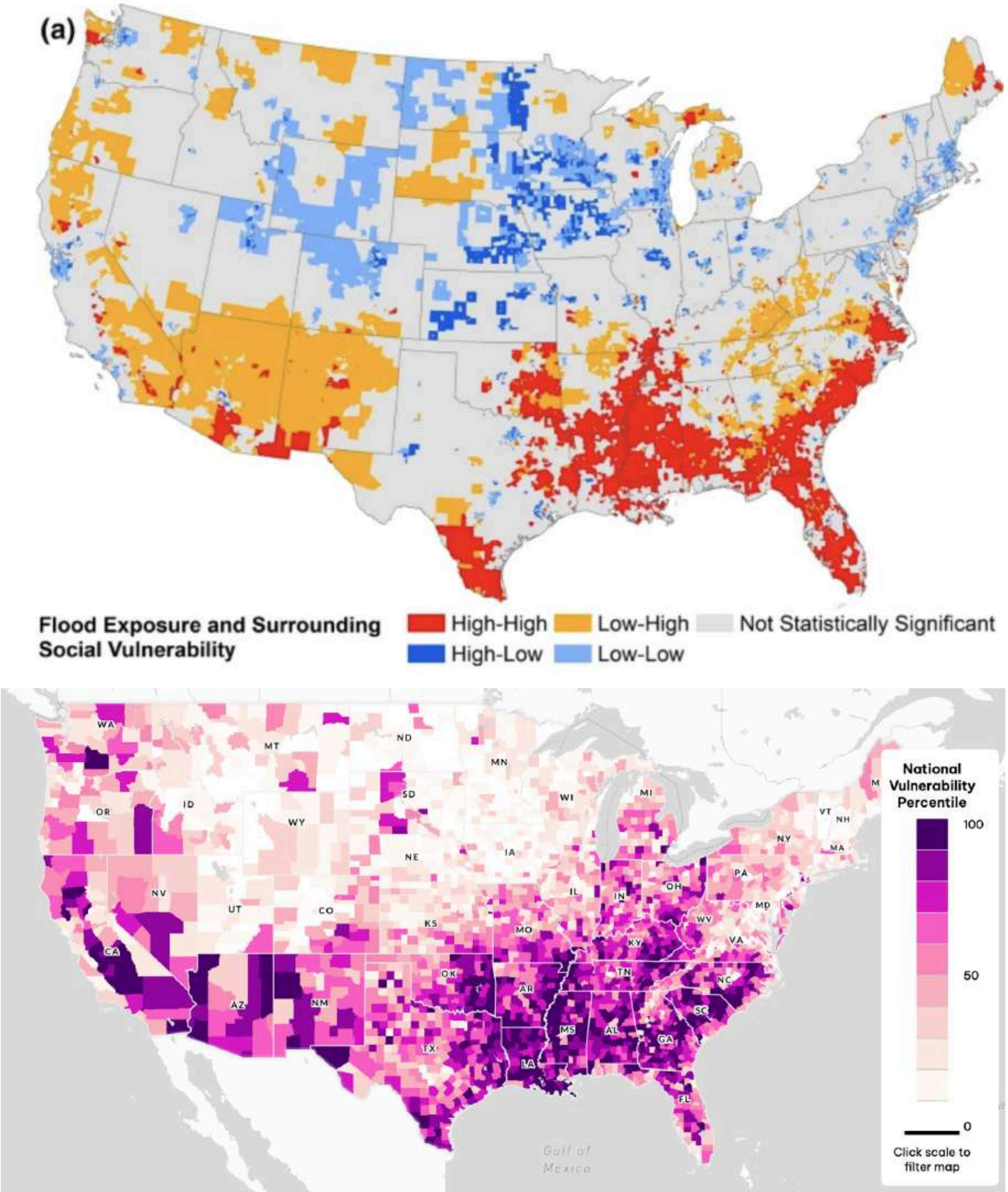

Figure 5.2 Top: showing Flood Exposure and Surrounding Social Vulnerability according to (Tate et al., 2021) and Bottom: Showing baseline vulnerabilities considering Health, Socioeconomic, Infrastructural, and Environmental Factors according to the US climate Vulnerability Index (Environmental Defense Fund, 2025)

Of the affected areas, Memphis stands out as a city with particularly low levels of green spaces, tree canopy coverage, but high rates of people living with disabilities (Wong et al., 2022). Evidence from non-affected areas suggest that distribution of new flood risk mitigating infrastructures in the form of green spaces is contextual with some cities prioritizing high income neighborhoods, while others are more equitable depending on the cities (Wong et al., 2022). In Louisville, particularly old grey infrastructure such as drainage systems to drain flood waters stem from as early as the 1800s is still in use causing large vulnerabilities to flash flooding, especially in historically redlined neighbourhoods with lower developed infrastructures (Office of Advanced Planning and Sustainability, 2020). Moreover, Louisville has a high risk of hazardous contamination of flood waters and a health care system that is ill prepared for emergencies (Office of Advanced Planning and Sustainability, 2020).

This rapid analysis does not allow for a closer investigation of all affected urban areas. But some progress can be seen, for example in the city of Springfield with substantial investments in green infrastructure to increase drainage of stormwaters (SBJ, 2024). In Huntsville, a variety of flood protection activities has been going on including flood mitigation plans adopted in 2001, modeling and mapping efforts of potential flood areas, clearing and transforming of identified high hazard areas to open green spaces and developing pilot flood emergency plans. Moreover, Development projects in floodplains need floodplain development permits and new building projects require flood proof building codes from 2018 and must be 1 foot above base flood levels. Still 70% of the city's wetlands have diminished since 1947 (City of Hutsville, nd).

Flood risk management

The US National Weather Service is responsible for providing early warning for both riverine and flash floods, with local NWS offices responsible for the counties in their respective forecast areas. The potential for flooding from this event was well-forecast with the US National Weather Service warning of potential generational flooding, as well as issuing flash flood emergency warnings, and tornado warnings across parts of Missouri, Tennessee, Mississippi, Kentucky, Illinois, Indiana, and Arkansas (US NWS, 2025; Reuters, 2025; Fox Weather, 2025). At least 6 National Weather Service offices were involved in warning about the event with warnings being issued up to a week before the riverine flood crests, giving sufficient time for local government and emergency responders to prepare (NWS, 2025).

State and local governments monitored the warnings and shared them with residents, and activated emergency operations centres to manage rescue and recovery efforts (TN, 2025). For example, in Kentucky fire trucks and emergency personnel were stationed in high risk areas, gas was preemptively shut off, and mandatory evacuation orders were issued for Butler and Falmouth towns (Hayes-Owen, 2025).

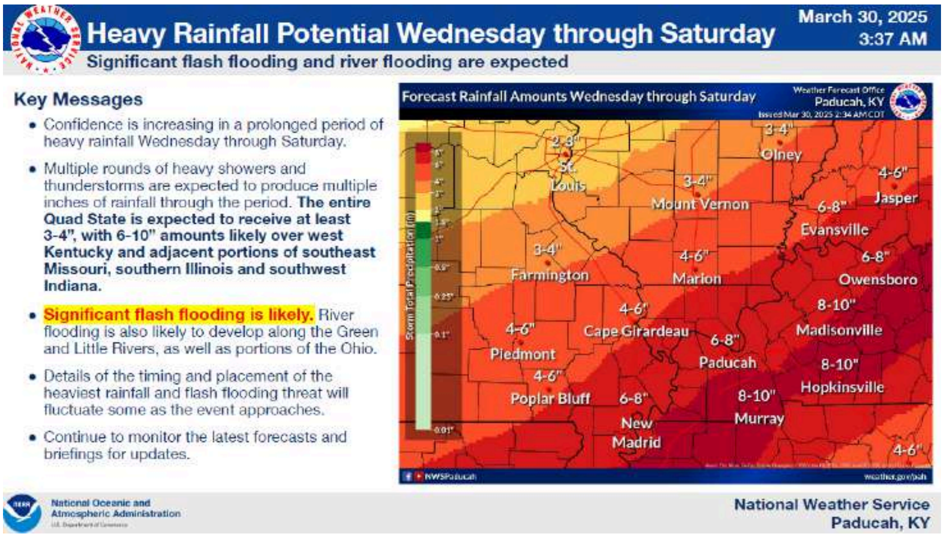

Figure 5.3: Example of a rainfall forecast with warning of flash flooding issued by the NWS Paducah, KY office on March 30, days in advance of the actual impacts.

Major disaster declarations were made for states including Arkansas, Kentucky and Tennessee, allowing for federal government support resources for the individuals affected by the severe storms. FEMA was supporting state and local efforts, including by coordinating the distribution of meals, water, and generators (FEMA, 2025). It also supported urban search and rescue efforts (FEMA, 2025). The storms also triggered NASA's Disaster Response Coordination System to support federal agencies in identifying damage, flood and landslide risk (Earth Observatory, 2025).

A review of 60 studies on community flood risk management in the USA revealed key lessons including recognising the importance of the conservation of wetlands as one of the most effective approaches to reduce flood losses and the importance of considering socially vulnerable populations in flood risk management programs (Tyler et al., 2019).

Finally, nearly half of NWS field offices are believed to have vacancy rates of 20% or more, double the short-staffing levels of a decade ago. (Borenstein, 2025). Former NWS leaders have warned that layoffs could impact the ability of NWS offices to respond to extreme weather events and keep people safe (Wholf, 2025).

V&E conclusions

The early April floods affected a large area in the middle of the Mississippi river basin, spanning at least 8 states. For agriculture, the impacts were a mixed bag, with some crops being spared given the early Spring timing of the floods, while others are damaged (e.g. wheat) or will require replanting (e.g. soybeans). Despite the historic nature of the rainfall and flooding, impacts on people were minimized as a result of sufficient early warning. Emergency managers were able to prepare communities by sharing warning messages, evacuating communities at highest risk, and closing roads or water systems to prevent worse impacts.

Data availability

All time series used in the attribution analysis are available via the Climate Explorer.

References

All references are given as hyperlinks in the text.

Appendix

A.1 Event definition sensitivity tests

Bigger box (82.5-92°W, 32-42°N)

Dataset	Event		Trend with GMST	
	Magnitude (mm)	Return period	Probability ratio (95% C.I.)	Change in intensity (%) (95% C.I.)
MSWEP	110.72	332.28 (42.04 - inf)	3.48 (0.06 - inf)	17.46 (-10.98 - 74.23)
CPC	94.88	292.55 (58.04 - inf)	0.78 (0.002 - 6.80)	-3.16 (-19.88 - 17.67)
ERA5	84.97	238.73 (42.12 - inf)	5.46 (0.95 - inf)	15.70 (-0.37 - 42.52)

Table A.1: Change in probability ratio and magnitude for rx4day in the larger central US region due to GMST. Light blue (orange) indicates an increasing (decreasing) trend that crosses no change, while dark blue indicates a statistically significant increasing trend. Statistically significant trends are also highlighted in **bold** font.

Sub-catchment

Dataset	Event		Trend with GMST	
	Magnitude (mm)	Return period	Probability ratio (95% C.I.)	Change in intensity (%) (95% C.I.)
MSWEP	240.17	132.32 (24.77 - 19575)	2.67 (0.93 - 247.46)	31.22 (-2.70 - 106.60)
CPC	216.05	158.73 (42.66 - 28358)	1.27 (0.16 - 4.13)	5.83 (-21.20 - 40.98)
ERA5	162.10	141.05 (23.82 - 10^8)	**15.95 (1.60 - inf)**	**36.66 (6.63 - 95.65)**

Table A.2: Change in probability ratio and magnitude for rx4day in a sub-catchment of the Mississippi river in the central US due to GMST. Light blue indicates an increasing trend that crosses no change, while dark blue indicates a statistically significant increasing trend. Statistically significant trends are also highlighted in **bold** font.

A.2 Circulation analogues

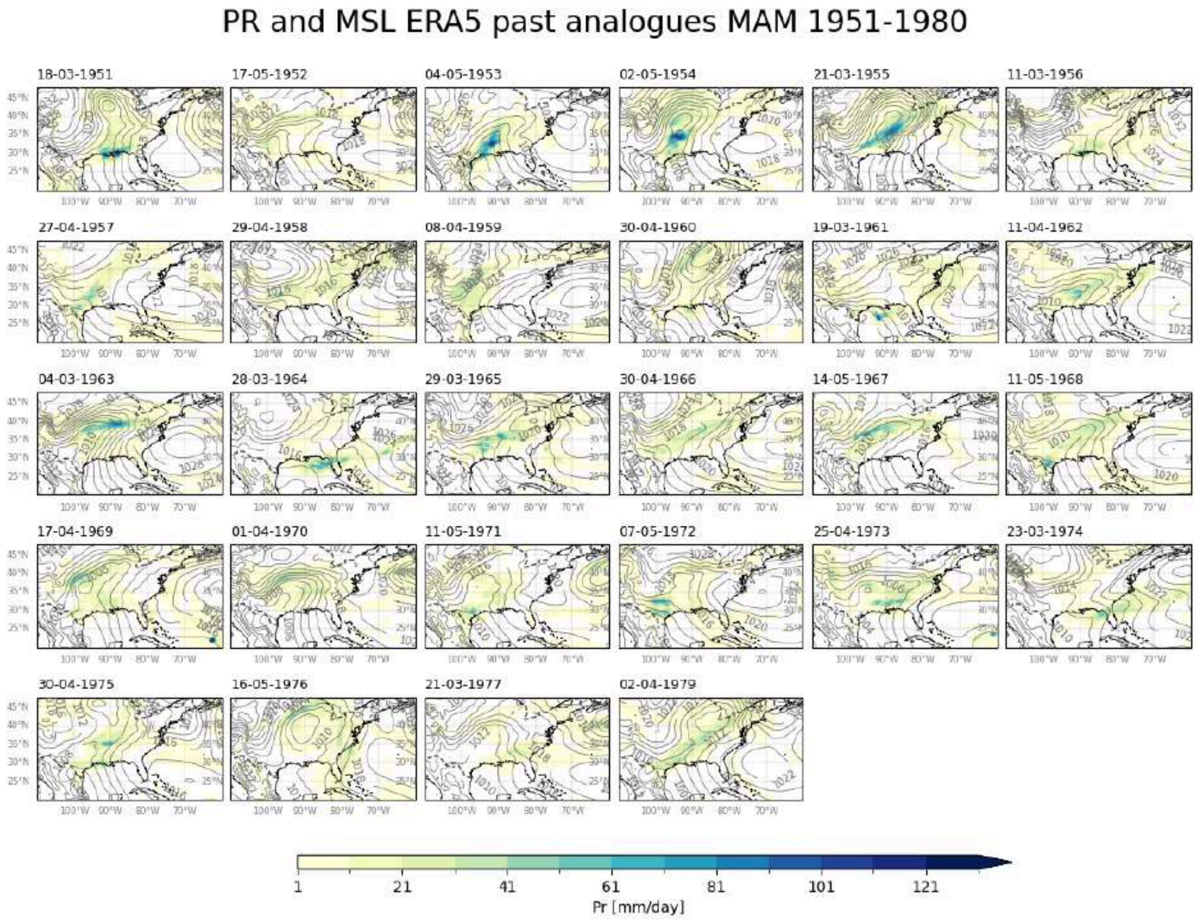

Figure A.3: *Rainfall and geopotential height for each of the analogues found over the period of 1951-1980.*

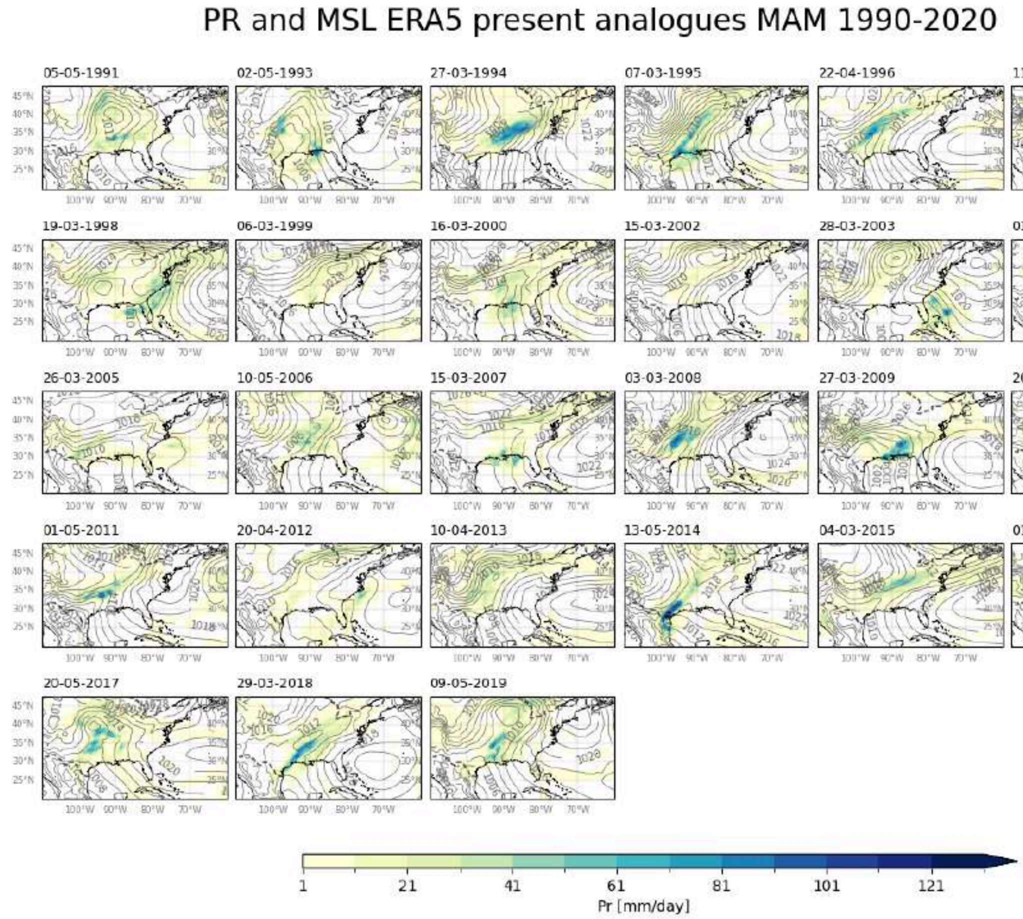

Figure A.4: *Rainfall and geopotential height for each of the analogues found over the period of 1990-2020.*

A.3 Model evaluation figures

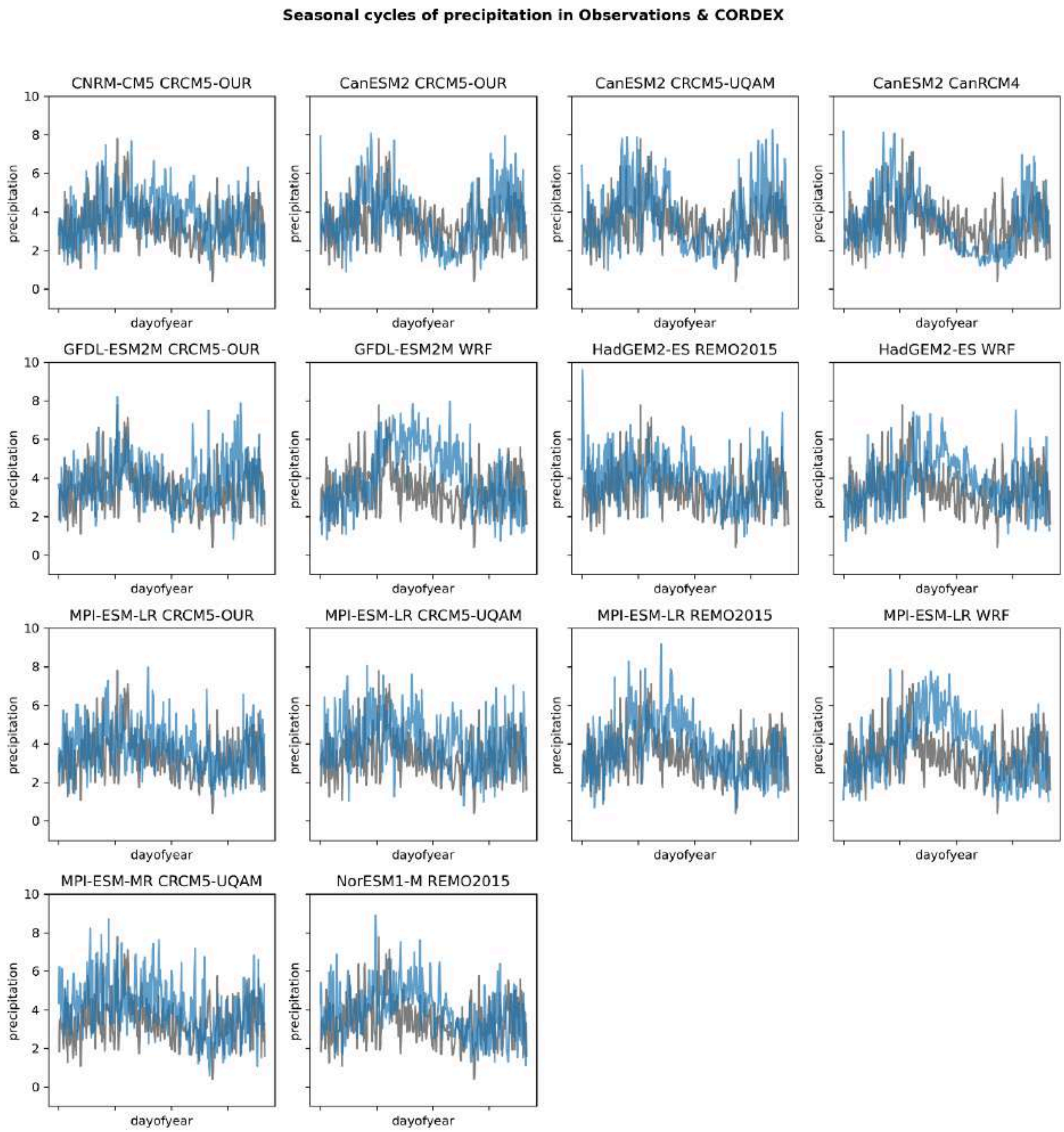

Figure A.5: *Seasonal cycles of precipitation in study region in observations and CORDEX models.*

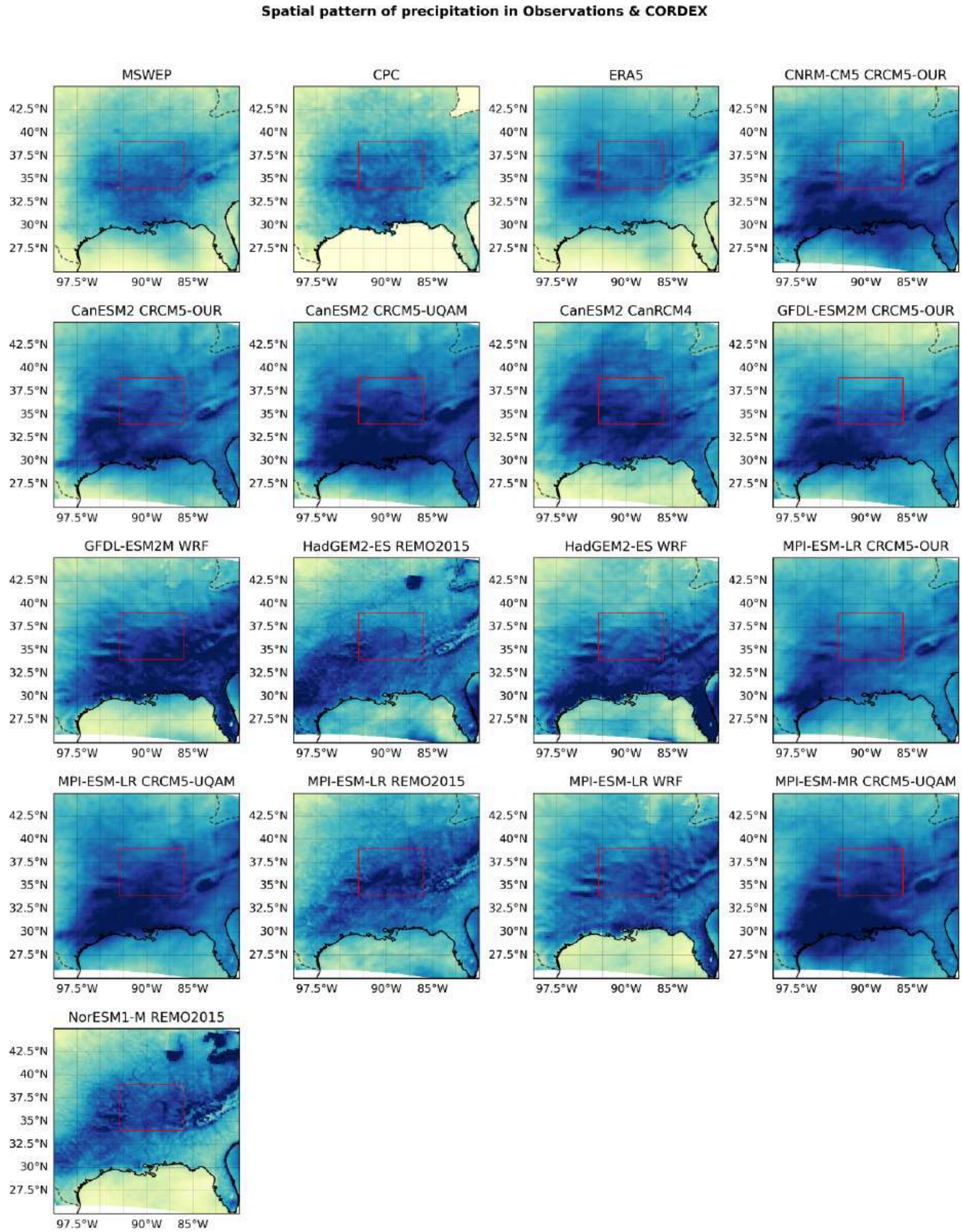

Figure A.6: *Spatial patterns of precipitation in March-May in observations and CORDEX models. The two study region is highlighted in red.*

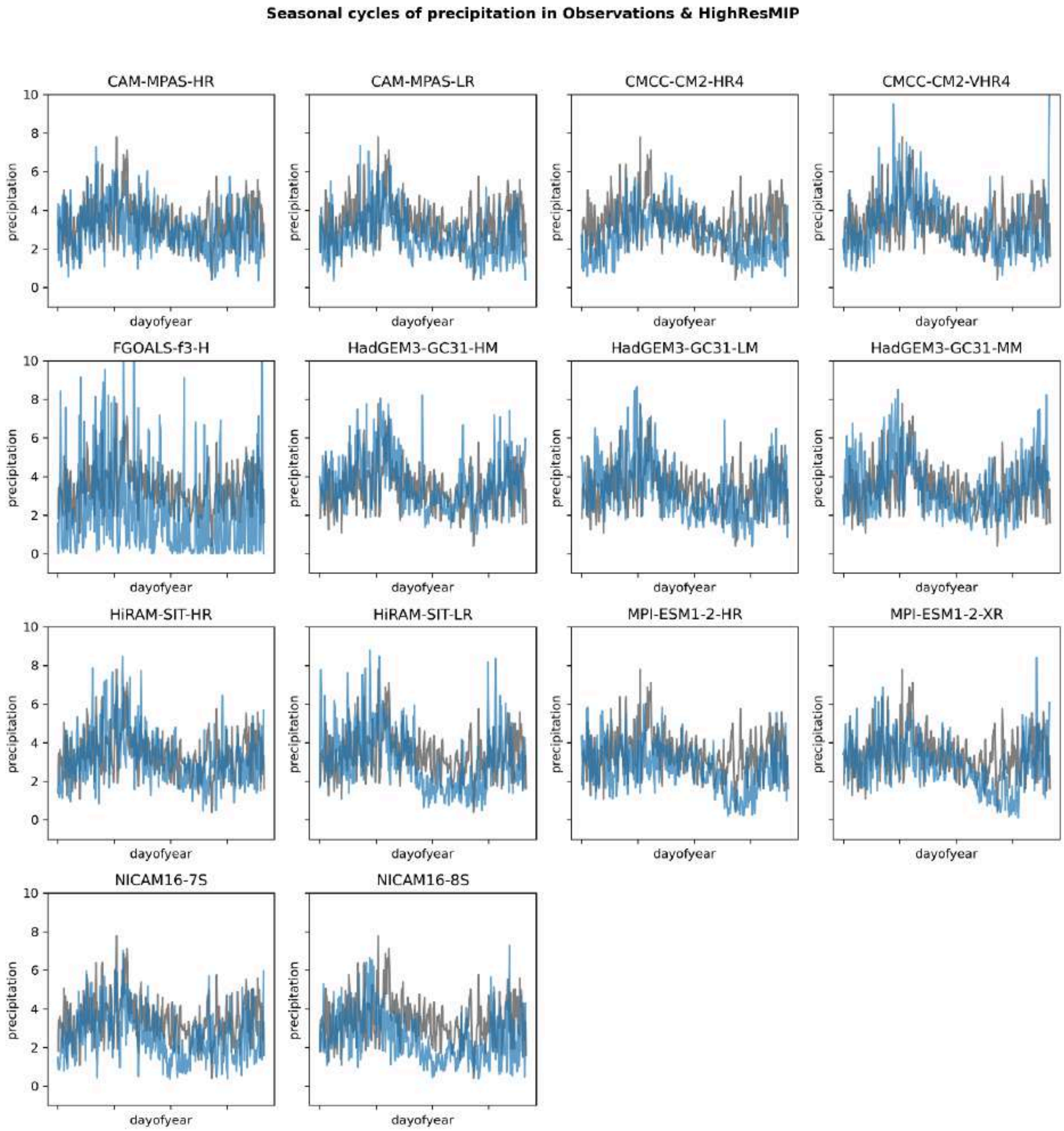

Figure A.7: *Seasonal cycles of precipitation in study region in observations and HighResMIP models.*

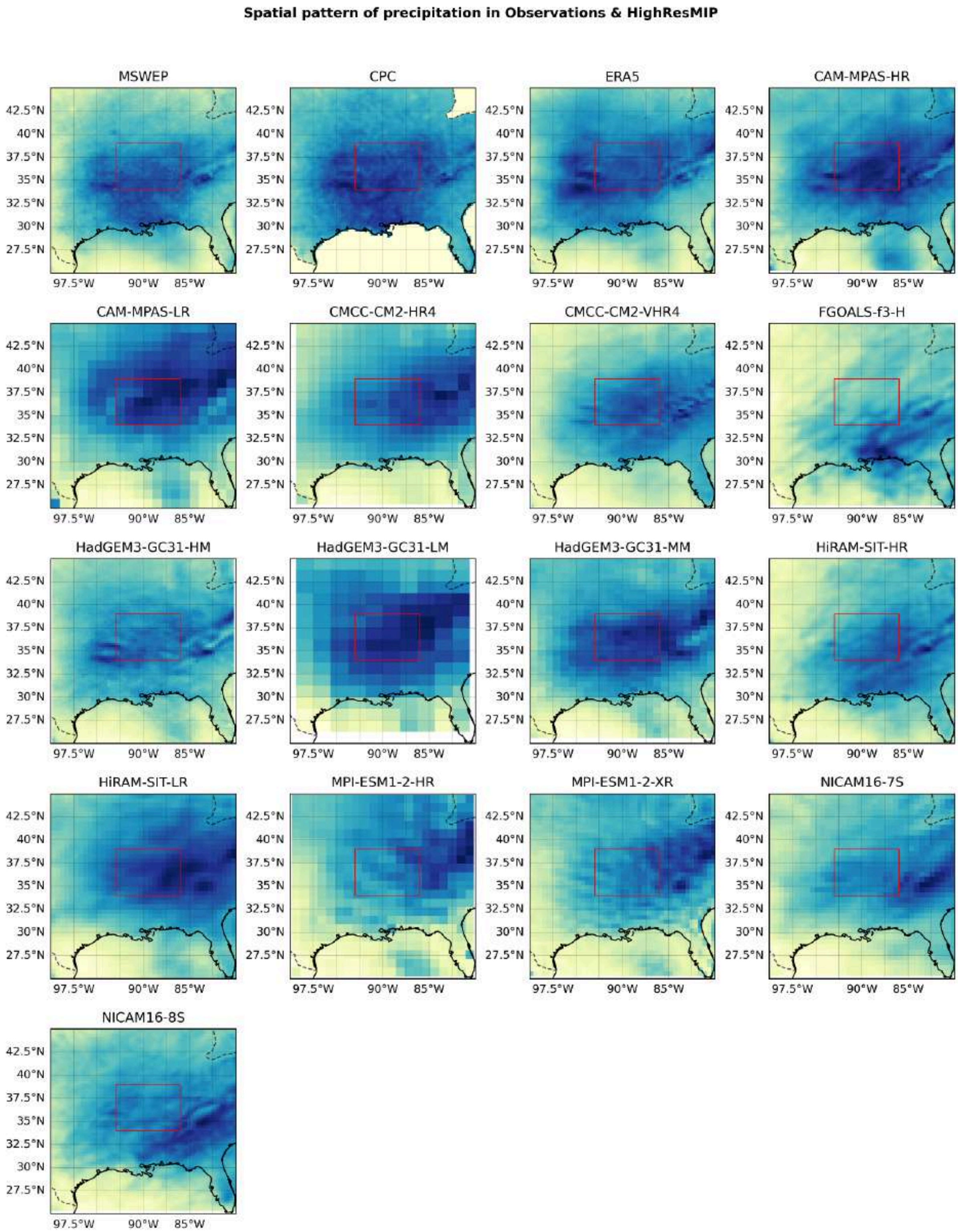

Figure A.8: *Spatial patterns of precipitation in March-May in observations and HighResMIP models. The two study region is highlighted in red.*

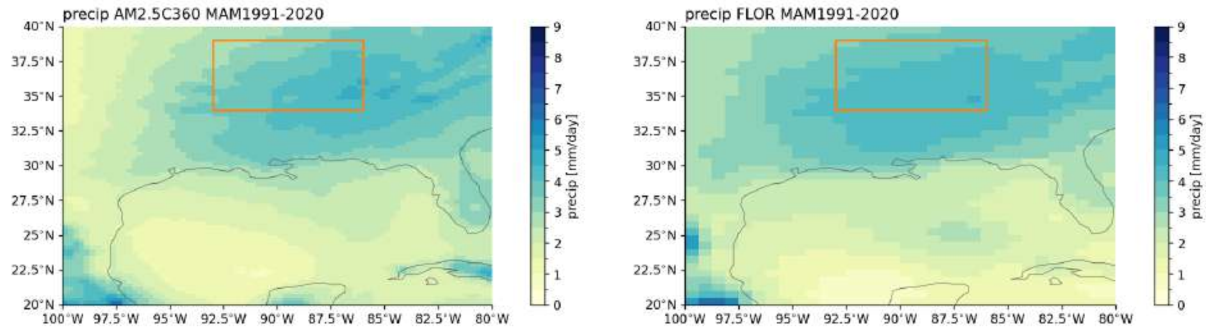

Figure A. : *Spatial patterns of precipitation in March-May in observations and AM2 (left) and FLOR (right) models. The two study region is highlighted in red.*

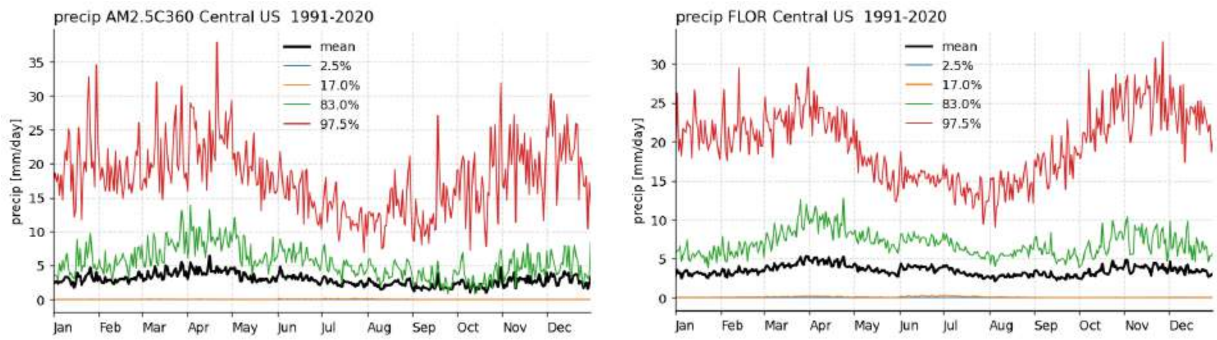

Figure A.9: *Seasonal cycles of precipitation in study region in observations and AM2 (left) and FLOR (right) models.*